



# **Diamond Film Structures for Secondary Electron Emission Applications**

Christine Hawkins

28<sup>th</sup> April 2017

This thesis is submitted in partial fulfilment of the requirements for  
the Honours degree of MSci Chemical Physics with Industrial  
Experience at the University of Bristol.



## Abstract

The possibilities of diamond's large secondary electron yield, as well as its other outstanding physical and chemical properties, present diamond as a very successful material for electron multiplication. A novel diamond film semiconductor-intrinsic-semiconductor (boron-doped diamond/i-diamond/boron-doped diamond) structure is investigated for transmission dynode applications. This p-i-p structure gives homojunctions for increased crystal quality on either side of the i-diamond film. BDD is itself used for secondary electron emission, which proves it a very interesting contact material. Unfortunately, SEE could not be confirmed from the radiation-detector proof-of-concept test. The proof of concept radiation tests showed a *decrease* in current on irradiation by Ni-63 beta-particles. An amplified signal - caused by extra carriers generated by the high-energy electron beam - would ideally be detected, with an increase in the current collected by the second electrode. The results did, however, correlate with previously found data regarding the p-i-p I-V diode behaviour. Further investigation is required to further this work. The process of fabrication of this structure is discussed and multiple structural and electrical characterisation techniques are shown. A growth rate of  $4 \mu\text{m h}^{-1}$  was achieved for deposition of undoped diamond, with uniform thicknesses and crystal sizes achieved. Raman spectroscopy showed peaks at  $1331.8 \text{ cm}^{-1}$  with FWHM values of ca.  $12 \text{ cm}^{-1}$ , which is on the order of values found in recent literature. A uniform boron-doped diamond layer was successfully deposited on the i-diamond exposed seeded-surface, with evidence shown by SEM imaging and Raman analysis. Some success of boron-doped diamond deposition on the growth surface of i-diamond was established, but further analysis would be required to confirm this. I-V characteristics of interim and final diamond film dynode structures were investigated, showing mostly ohmic behaviours. One sample showed a diode I-V curve characteristic, explained by the p-i-p diode structure and the nitrogen impurities inducing donor-like traps at the i-diamond interface.

There were difficulties throughout the project, regarding fragility of the samples and ability to grow uniform BDD layers on the growth surface of the i-diamond layer. Selective growth of BDD in the HF-CVD reactor showed promise, however it did not solve the issue of surface conduction. Due to surface conduction, the final structure samples did not merit testing for radiation detector behaviour; however, the interim structure samples worked successfully as radiation detectors. Methods of each fabrication process were optimised and a successful method of handling the films was established.



## Acknowledgements

I would like to say the biggest thank you to all the people who helped me with this project; my supervisor Dr. Neil Fox, my PhD supervisor Alex Croot, and Dr. James Smith for their amazing support and guidance throughout.

I would like to say thank you to everyone who I spent time with in the Diamond Lab, for making my time fun and knowledgeable.

A final thank you to my dearest family and friends.



# Contents

---

Abstract.....	3
Acknowledgements.....	5
1 Introduction .....	9
1.1 Preface.....	9
2 Theory.....	10
2.1 Secondary Electron Emission (SEE).....	10
2.1.1 Generation of Internal Secondary Electrons.....	10
2.1.2 Transport of Internal Secondary Electrons to the Surface .....	11
2.1.2.1 Townsend avalanche.....	12
2.1.3 Escape to anode and then over vacuum barrier.....	13
2.1.4 Surface terminations.....	15
2.1.4.1 Negative Electron Affinity (NEA).....	15
2.1.4.2 O-Termination.....	17
2.1.5 Primary Electron Source.....	17
2.1.6 Applications of Electron Multiplication .....	17
2.1.6.1 Radiation detectors.....	17
2.1.7 Devices used today.....	18
2.1.7.1 Micro-channel plate (MCP).....	18
2.1.7.2 PMT.....	19
2.2 Dynodes .....	19
2.2.1 Introduction to Dynode.....	19
2.2.2 Reflection and Transmission: Dynode Macrostructure Within EM Device..	19
2.2.3 Materials used for bulk material/central layer .....	21
2.2.4 Electronic Contacts .....	21
2.3 Diamond.....	22
2.3.1 Diamond Structure.....	22
2.3.2 CVD Diamond For Dynode Applications .....	24
2.3.2.1 Defects / Traps.....	24
2.3.3 Diamond Quality .....	25
2.4 Diamond Growth Techniques.....	26
2.4.1 HPHT .....	27
2.4.2 CVD.....	28
2.4.2.1 Chemical Reactions in the CVD Reactor.....	30
2.4.2.2 HF-CVD .....	30
2.4.2.3 MW-Plasma CVD .....	31
2.4.2.4 Boron Doping.....	31
2.4.2.4.1 Surface States .....	32
3 Experimental Methods .....	33
3.1 Diamond Film Dynode .....	33
3.1.1 Novel Structure.....	33
3.1.1.1 Explanation of the Layers.....	33
3.1.2 Fabrication of the Samples .....	34
3.1.2.1 Nucleation of Substrates.....	35
3.1.2.2 I-Diamond Layer Growth.....	35
3.1.2.3 Laser Etch of Silicon Substrate.....	36
3.1.2.4 Wet Etch of Silicon Substrate.....	36
3.1.2.5 Boron Doped Diamond (BDD) Layer Growth .....	36
3.1.2.6 Boiling Acid Clean (H <sub>2</sub> SO <sub>4</sub> , KNO <sub>3</sub> ).....	37
3.1.2.7 Electrical Contact For Testing Purposes.....	37
3.2 Structural Characterisation Techniques and Equipment.....	38

3.2.1	Scanning Electron Microscopy.....	38
3.2.2	Raman Spectroscopy.....	38
3.2.3	Laser Micro-Machining System.....	39
3.3	Electrical Characterisation.....	39
3.3.1	High resistance, I-V Curves.....	39
3.3.2	Radiation Detector Behaviour.....	40
4	Results and Discussion.....	42
4.1	Structural Characterisation.....	42
4.1.1	Scanning Electron Microscopy (SEM) Characterisation.....	42
4.1.2	Raman Spectroscopy Analysis.....	47
4.2	I-V Characteristics.....	50
4.2.1	Diode Behaviour.....	52
4.3	i-Diamond/n-Si Radiation Detector Behaviour.....	53
4.4	Conclusion.....	55
5	Future Work.....	56
6	References.....	57

# 1 Introduction

## 1.1 Preface

Diamond and thin diamond films are considered the best choice for electronic high-temperature applications and of radiation resistant materials, due to their outstanding physical and chemical properties. These properties include extremely high chemical and radiation stability, highest thermal conductivity and highest mobility of carriers of known materials. Diamond's large band gap specifically provides the basis for its use in electron multiplication applications as it provides a large secondary electron yield (SEY). This will be exploited to investigate a thin film diamond structure for use in dynode applications in photo multiplier tubes (PMT).

## 2 Theory

### 2.1 Secondary Electron Emission (SEE)

When high-energy charged particles bombard the surface of a solid, electrons are emitted from the solid. This is the process of secondary electron emission<sup>1,2,3,4</sup>. Where the bombarding particles are electrons, the incident and emitted electrons are called primary and secondary, respectively. This process is very important to the function of vacuum electronic devices. In some cases, researchers attempt to select materials to reduce secondary electron emission, whilst in others the goal is to enhance it. High secondary electron emitters are desirable when electron multiplication, or signal amplification, is required, such as in photomultiplier tubes, crossed-field devices and radiation detectors. When a material has been optimised for secondary electron emission, every primary electron or incident charged particle induces the production of > 1 secondary electron, resulting in a gain of electrons on collision with the material – the secondary electron yield (SEY). Secondary electron emission can be applied across multiple gain stages; acceleration of these secondary electrons by means of an electric field towards further gain stages produces exponential amplification.

The secondary electron emission characteristics of a material are described by the secondary electron yield (SEY) and the energy distribution of the emitted electrons. These characteristics are dependent on both the incident electrons and the properties of the material itself. The SEY coefficient,  $\delta$ , is defined as the number of secondary electrons released from the surface divided by the number of incident primary electrons. This is most easily shown in terms of current:

Equation 2.1

$$\delta = \frac{I_s}{I_p}$$

Where  $I_s$  is the secondary current and  $I_p$  is the primary current.

The SEE process can be split into three steps: (1) generation of internal secondary electrons by kinetic impact of primary electrons; (2) transport of internal secondary electrons through sample bulk towards the surface, and (3) escape of electrons through the solid-vacuum interface.

#### 2.1.1 Generation of Internal Secondary Electrons

Primary electrons bombarding the surface penetrate the material and lose fractions of their energy through collisions with ions and electrons within, creating electron/hole pairs. Creation of these electron/hole pairs occurs when an electron in the bound ground state (in the valence band) is promoted to the conduction band, leaving a hole in the valence band. As previous research has shown, most secondary electrons are generated within a small range of the primary electron's penetration depth. This is due to the slower movement of the electron at the end of its path giving greater time for its interaction with valence electrons<sup>5</sup> (see Figure 2.1). Following the derivations of Dvorkin *et al.*, on average, a primary electron will use thrice the band gap,  $E_g$ , of the material of its energy for electron/hole pair generation<sup>6</sup>, (other sources state a value of 2.5 times the  $E_g$ <sup>7</sup>) therefore the internal yield can be approximated to be  $E_0/3E_g$ <sup>8</sup>. For diamond these values depend on the quality and crystal class – thrice the band gap of diamond gives 16.41 eV, whereas polycrystalline diamond requires ca. 19 eV to excite one electron/hole pair, and single crystal diamond requires ca. 13 eV. As the incident

energy of a primary electron increases, it can generate more secondary electrons as it has more kinetic energy to transfer to the system, however, these secondary electrons will originate deeper within the material, as can be seen in Figure 2.2.

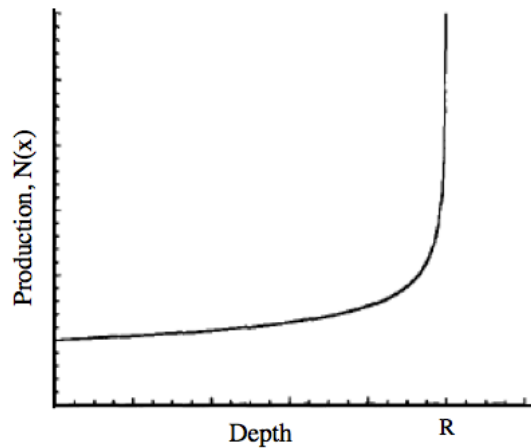


Figure 2.1: Production rate of internal secondary electrons as a function of distance along the path of the primary electron, adapted from reference [9].

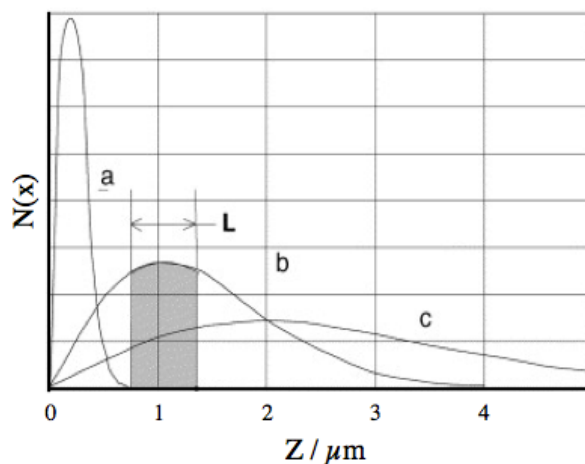


Figure 2.2: Distribution of the stopping points of primary electrons of differing primary energies; (a) 10 keV, (b) 20 keV, (c) 30 keV.  $L$  is the relative carrier diffusion length, adapted from reference [10].

### 2.1.2 Transport of Internal Secondary Electrons to the Surface

Internally generated secondary electrons gain kinetic energy when colliding with other primary electrons. In the bulk, internally generated secondary electrons transfer their kinetic energy by creating additional electron/hole pairs, or by colliding with phonons. The movement of the secondary electrons through the bulk can be modelled by two methods: a single-scattering process, or a diffusion process that involves a large number of scattering events. Later models have included the electron multiplication cascade – occurring during the slowing down of the internal secondary electrons – which is a similar process to the gas ionisation in the Townsend Avalanche (see Section 2.1.2.1) In all of the models, the escape of secondary electrons from the bulk is characterised by an exponential decay law where they have a characteristic escape depth.

Historically, the main mode of secondary electron emission works in reflection mode, when the primary electrons bombard the same surface from which the secondary electrons are emitted. Therefore, the distance within the material that secondary

electrons originate is important; secondary electrons that have been generated deeper in the material will require more energy to escape. Recently, transmission secondary electron emission is being researched as the next development in electron multiplication devices. In this case, depending on the thickness of the material upon which primary electron bombardment takes place (material in which secondary electron generation occurs), a bias may be required to pull electrons through to the opposite surface. If the material is thin enough, when it is roughly equivalent to the penetration depth of primary electrons plus the escape depth of the secondary electrons, a bias is not required.

When a material undergoes continuous secondary electron emission with a gain greater than unity, there will be a net electron flow from the material to vacuum. Some form of electrical conductivity is necessary to replenish electrons lost in the process; as otherwise, charging of the sample will decrease the secondary electron yield to 1. There are different approaches to introducing a source of electrons to the system. In an oxidised beryllium based SEE set-up, the thin BeO (1 – 2 nm) layer is supported on metallic Be. In a magnesium oxide / gold cermet SEE set-up, the Au particles provide the conduction path<sup>11</sup>. A bias can also be used to provide an increase in carriers.

Generally, a primary electron will generate a great number of secondary electrons, as shown by Equation 2.1: a primary electron with incident energy of 3 keV striking a material with band gap of 1 eV will generate ~ 1000 secondary electrons. However, high secondary electron yields are rarely observed due to energy losses to the system, leaving secondary electrons with energies below the vacuum level and therefore unable to escape.

Energy loss mechanisms differ between metals and insulators. In metals, the primary loss mechanism is through electron-electron interactions as there are many electrons in the conduction band; others are interactions with lattice vibrations and defects. For a secondary electron to escape the material, it must have energy equal to or greater than the sum of the Fermi level plus the work function, and this is typically ca. 10 eV. This large minimum escape energy combined with the high probability of collisions due to large number of conduction band electrons results in a small SEY in metals. The maximum yield for metals varies between 0.5 (for Li) and 1.8 (for Pt), averaging ca. 1<sup>12</sup>.

In insulators and semiconductors, the minimum escape energy is the electron affinity – the difference between the conduction band minimum and the vacuum level – usually ca. 1 eV. Due to few conduction band electrons, the main secondary electron energy loss mechanism is through further ionisation events. The wide band gap prevents secondary electrons with energies lower than the band gap participating in these collisions. For these lower energy secondary electrons, the main processes for energy loss are electron-phonon and electron-impurity collisions. Because of this lack of electron-electron scattering in the conduction band, secondary electrons lose much less energy as it moves through the material, increasing its escape depth. Therefore, it is common for insulators to have high SEY. The maximum yields for NaCl is 6.8, and 25 for single-crystal MgO<sup>13</sup>. E. Wang *et al.* demonstrated an emission gain up to 178 in H-terminated diamond<sup>14</sup>.

#### 2.1.2.1 Townsend avalanche

Townsend Avalanche occurs within the medium between two electrodes of high potential difference. Within a semiconductor medium, the generation of an electron/hole pair, which can be described as an ionisation event, can lead to avalanche breakdown. This is when the field accelerates the first carriers, increasing their kinetic

energy, which on collision with valence band electrons leads to further ionization events. As all of these secondary electrons are within a high electric field, this will lead to a chain reaction called the Townsend avalanche<sup>15</sup>. Initially, the number of secondary electrons grows exponentially, until it reaches a limit known as the Raether Limit, due to the effect of the space charge on the electric field<sup>16</sup>. This process of induced electron multiplication by electric field depends on the thickness of the semiconductor medium and the strength of the electric field. If the material is too thin or the electric field too weak, a secondary electron will not gain enough kinetic energy to induce further ionisation events<sup>17</sup>. However, if the material is too thick, the necessity of a higher applied voltage would risk electrical breakdown effects.

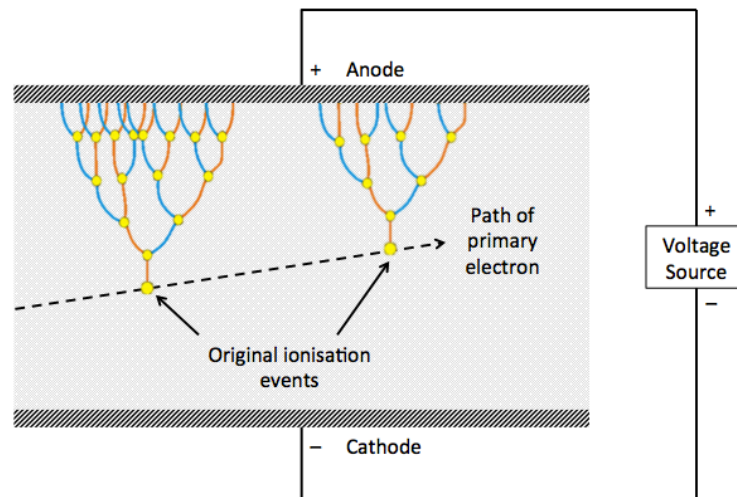


**Figure 2.3: Visualisation showing how an original primary electron causes ionisation events within a medium biased under an electric field can lead to Townsend Avalanches. The yellow circles indicate ionisation events, the orange lines liberated electron paths and the blue lines ionising electron paths, adapted from reference [18].**

### 2.1.3 Escape to anode and then over vacuum barrier

After secondary electron generation has occurred and these electrons have undergone multiple energy-loss mechanisms, as discussed in Section 2.1.2, secondary electrons will have been thermalized and therefore sit in high concentration at the bottom of the conduction band. To escape, they must overcome the potential barrier – the work function for metals, and electron affinity for semiconductors and insulators, see Figure 2.7. Many theories regarding secondary electron emission do not place importance on the process of escape at the solid-vacuum interface. Bouchard and Carette<sup>19</sup> found that the energy barrier at the interface controls the distribution of the secondary electron emission energy. However, this model along with others did not observe the vacuum-barrier height as having an impact on the magnitude of SEY. Jenkins and Trodden<sup>20</sup> showed that by using Na-termination on W, they reduced the work function by 3 eV and increased the SEY by 60 %. Diamond does not correspond to these conventional models, however, as its H-termination causing a vacuum-level lowering of 1.45 eV increases the SEY by more than an order of magnitude.

Incredibly high SEY magnitudes for H-terminated diamond were reported in the 90s<sup>21,22,23,24</sup>, with a gain of up to 86 shown<sup>25</sup>. There are two key reasons for this high SEY in diamonds. The first of which is the wide band gap leading to a larger escape depth of secondary electrons (explained in Section 2.1.2). The second is the possibility for low or negative electron affinity, which allows the concentrated thermalized electron energy

distribution at the bottom of the conduction band to escape<sup>26</sup>. Photoemission energy distribution curves of diamond show that a high percentage of electrons reside in the lowest conduction band, meaning they have very low energy<sup>27</sup>, as shown in Figure 2.4. H-termination causing NEA is therefore crucial to diamond's large SEY, as without it, only the few non-thermalised electrons can be emitted. It also results in emitted electron beams with a low energy spread.

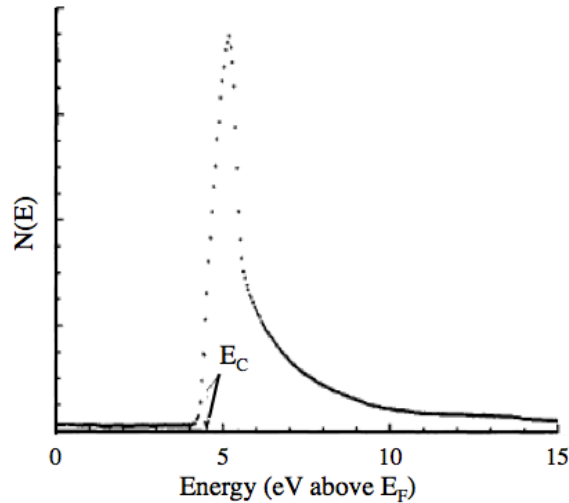


Figure 2.4: Secondary electron energy distribution curve (EDC) of a H-terminated, boron-doped diamond sample. The energy is represented relative to the Fermi-level. Primary electron energy of 1 keV, adapted from reference [28].

It is shown in Figure 2.5 that loss of H-termination by desorption by heat treatment increases the vacuum height by about 1.45 eV and is therefore too high for the low-energy electrons to escape. Figure 2.6 shows the loss in SEY after heat-treatment of the sample. This indicates the requirement for a stable NEA surface.

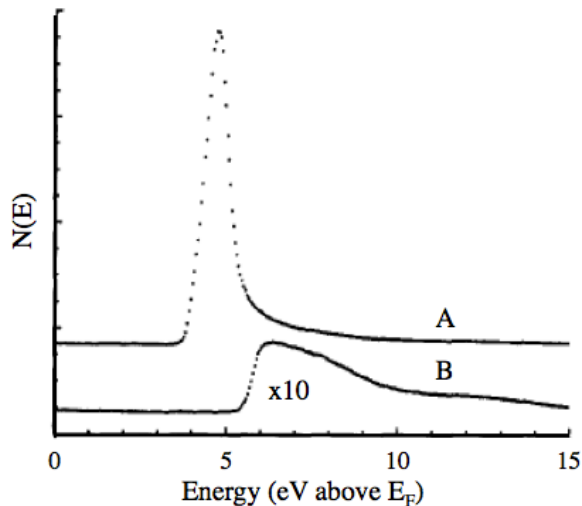


Figure 2.5: Change in secondary electron energy distribution curve of a H-terminated boron-doped diamond sample after 1000 °C heating. (A) is before heating, (B) is after heating, adapted from reference [29].

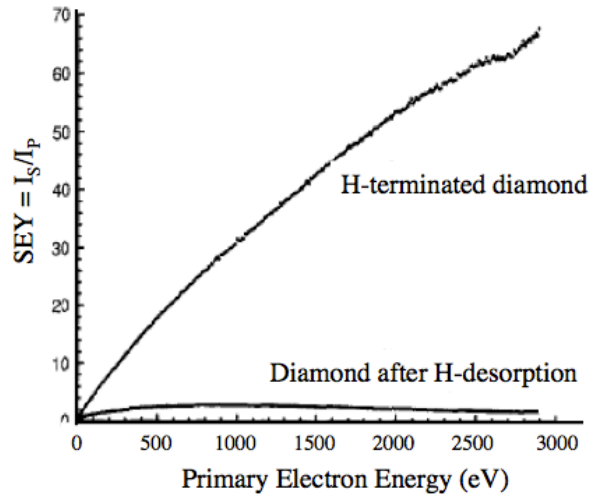


Figure 2.6: A large reduction in SEY is shown on H-desorption from the diamond surface, adapted from reference [30].

## 2.1.4 Surface terminations

### 2.1.4.1 Negative Electron Affinity (NEA)

Electron affinity is defined as the energy required to remove an electron from the conduction band minimum to a distance macroscopically far from the material. At the surface this can be shown as the difference between the conduction band minimum and the vacuum level<sup>31</sup>. A strategy used for increasing SEY is the introduction of a negative electron affinity (NEA) by proper surface termination. This is the introduction of a monolayer of atoms onto the surface<sup>32</sup>. An NEA is when the vacuum energy lies lower than the conduction band minimum – making ejection of secondary electrons from the surface energetically favourable<sup>33</sup>, as shown in Figure 2.7. NEA can be achieved by H-termination of diamond, or Cs and Cs-O-terminations on semiconductors in general.

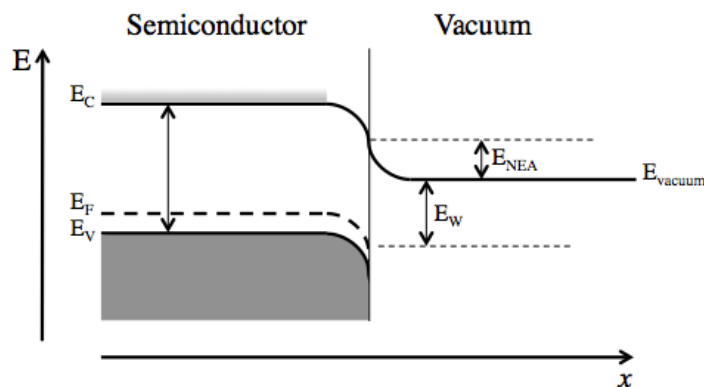
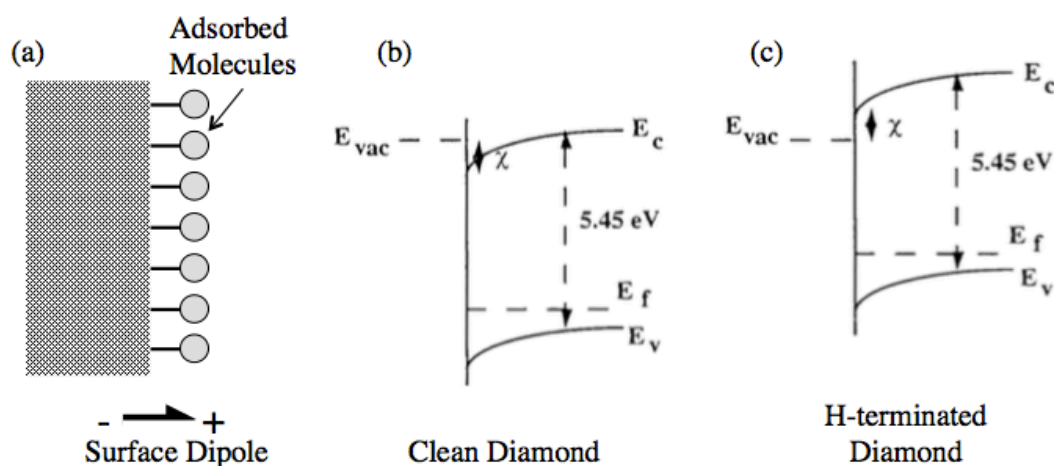


Figure 2.7: General band diagram of a semiconductor-vacuum interface showing negative electron affinity  $E_{NEA}$ , defined as the difference between near-surface conduction band minimum  $E_C$ , and near-surface vacuum energy  $E_{vacuum}$ . Fermi level  $E_F$ , valence band maximum  $E_V$ , work function  $E_w$ . Produced with reference to [34].

Hydrogen-terminated diamond has a conduction band minimum at  $\sim 1.1$  eV above the vacuum level<sup>35</sup>, corresponding to the value of  $E_{NEA}$  in Figure 2.7. The electron affinity is ascribed to two aspects; (1) the origin of the atomic levels, which are generally intrinsic to the material; and (2) the termination-induced surface dipole, which is significantly affected by surface reconstructions and adsorbates. The H-termination changes the

surface dipole, which results in a downward shift of the energy bands with respect to the vacuum level, as shown in Figure 2.8. This surface dipole is due to the difference in electronegativity in the surface C-H covalent bonds. Dipoles are induced on the surface – with a slight positive charge,  $\delta+$ , on the hydrogen atoms, just outside the surface of the diamond. This attracts electrons within the material out to the  $\delta+$  positive hydrogen atoms.



**Figure 2.8:** (a) A representation of the effect of surface termination to a material, introduction of a surface dipole. The band alignments on boron doped diamond samples: (b) Clean diamond (111); (c) H-terminated diamond (111), adapted from reference [36].

It is important to consider the limitations of surface terminations. For certain terminations, the device has to be made and operated in a vacuum environment because the terminations are reactive when exposed to air. This is especially true when using Cs. Alternative terminations, such as Li-O and Mg-O, have been observed as air-stable on diamond<sup>37,38</sup>. H-terminated diamond was proven successful for diamond transmission dynodes in 2010<sup>39</sup>. The layer was extremely robust, with no degradation during the emission process, and only decreased to 50 % of its original SEY after 6 months' exposure to air. In vacuum, the surface had high thermal and chemical stability due to the strong C-H covalent bond, even after exposure to over 400 °C<sup>40</sup>. In general, a H-terminated surface is stable and robust in a practical operating environment, as it is stable in vacuum up to 800 °C and the NEA property can be restored after exposure to air by annealing at ca. 400 °C to remove surface adsorbates<sup>41</sup>. High-energy electron impact also degrades H-terminated surfaces. For applications where a high-energy electron beam is required to be incident on an NEA surface, strategies are being explored to overcome this challenge. For example, a robust, air-stable NEA surface of lithium-covered O-terminated diamond has been demonstrated which exhibits the same high emission efficiency as the H-terminated surface<sup>42</sup>. Another strategy that is employed in this study is the transmission approach (see Section 2.2.2).

A risk of some surface terminations when exposed to air for extended periods of time is the possibility of adsorbates altering the surface characteristics of the material, such as hydrogen-related species which can increase the surface conductivity. Hole surface conductivity can also be exhibited, which is ascribed to electro-chemical charge transfer from molecular adsorbates<sup>43,44</sup>. Annealing or other surface treatments can resolve this<sup>45,46</sup>.

#### 2.1.4.2 O-Termination

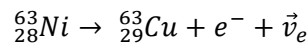
Oxygen-termination, on the other hand, correlates with a positive electron affinity (PEA) due to the surface dipole this creates. The more electronegative O induces a  $\delta^-$  on the oxygen surface layer, acting as a barrier to keep the electrons within the surface. While H-termination is achieved by exposing the diamond surface to hydrogen plasma, O-termination can be achieved by treating in oxygen-plasma or by boiling in strong acid. In contrast to a H-terminated diamond surface, an O-terminated diamond surface is strongly resistive<sup>47,48</sup>.

#### 2.1.5 Primary Electron Source

The most common electron source for bombardment of material is a photocathode; as for most signal amplifications the source is a photon source. This is seen in photomultiplier tubes and micro-channel plate multipliers alike. For certain applications, the primary electron source would not be photons but radiative particles, such as beta, gamma and alpha radioisotope sources. Beta-decay is an active research topic regarding secondary electron emission for beta-batteries<sup>49</sup>. These aim to use diamond-encapsulated C-14 from nuclear plant waste, to create extremely long-lived batteries – on the order of the lifetimes of the radioactive isotope.

Ni-63 is a good beta-particle source, with maximum emission energy of 67 keV and average emission energy of 17.43 keV, making it a low energy beta source. Beta-decay occurs when a neutron in the atom decays into a proton, an electron and an anti-neutrino (see Equation 2.2). In the macroscopic material, the rate of decay is highly predictable, with a well-referenced half-life of 100.1 years<sup>50</sup>.

#### Equation 2.2



#### 2.1.6 Applications of Electron Multiplication

Electron multiplication is useful in many applications where amplification of electron or photon (by use of a photocathode via) signals is required, including camera devices, radiation detectors and laboratory/medical analysis devices.

**Table 2-1: A few examples of the applications of electron multiplication.**

Application	Author	Year
Photomultiplier tubes	H. Semat et al. <sup>51</sup>	1972
Radiation sensors	P. Bergonzo et al. <sup>52</sup>	2001
Cold cathodes	P.K. Baumann et al. <sup>53</sup>	2000
Bio-sensing	C.E. Nebel et al. <sup>54</sup>	2007
Electron multiplication	D.M. Trucchi et al. <sup>55</sup>	2006
Image intensifier tubes	M.L. Perl et al. <sup>56</sup>	1964

##### 2.1.6.1 Radiation detectors

Diamond has remarkable electronic properties including high carrier mobility, a wide band-gap, radiation hardness and a high breakdown voltage<sup>57</sup>. These properties of diamond have been known and used since the 1950s as natural single crystal (sc) diamond for radiation detectors. Many papers report a charge collection efficiency (CCE)

close to 100 %<sup>58</sup> from their diamond radiation detectors. An advance in diamond detectors in 2002 occurred when Element 6 reported synthetic growth of single crystal CVD electronic grade (sc-CVD-EG) diamond, showing extraordinary long lifetime and very high mobilities of charge carriers<sup>59</sup>. Since that report, sc-CVD-EG diamond detectors have been successfully developed for uses in many large physics experiments; such as beam loss monitors in the Large Hadron Collider<sup>60</sup>; as fast start detectors in GSI (a heavy ions accelerator)<sup>61,62</sup>; and as semi-transparent x-ray beam monitors in many synchrotrons across the globe<sup>63,64,65</sup>.

### 2.1.7 Devices used today

There are a few common geometries of devices for electron multiplication used today.

#### 2.1.7.1 Micro-channel plate (MCP)

A modern imaging device that makes use of SEE is the micro-channel plate multiplier (MCP). It consists of an array of millions of single channel capillary electron multipliers (of internal diameter ca. 10  $\mu\text{m}$ ), in a glass plate of thickness ca. 1 mm; see Figure 2.9, (a). The capillaries are internally coated with a secondary electron emissive material, often a semiconductor, enabling them to behave as a continuous dynode, multiplying the electron current inputted at that position (see Figure 2.9, (b)). The faces of the plate are coated with thin metal films to act as electrodes with a voltage applied across them. This device therefore gives good spatial resolution, as the local photon flux can be rapidly converted into an electron flux that can be measured directly<sup>66</sup>. Therefore MCPs can be used in position-sensitive detectors.

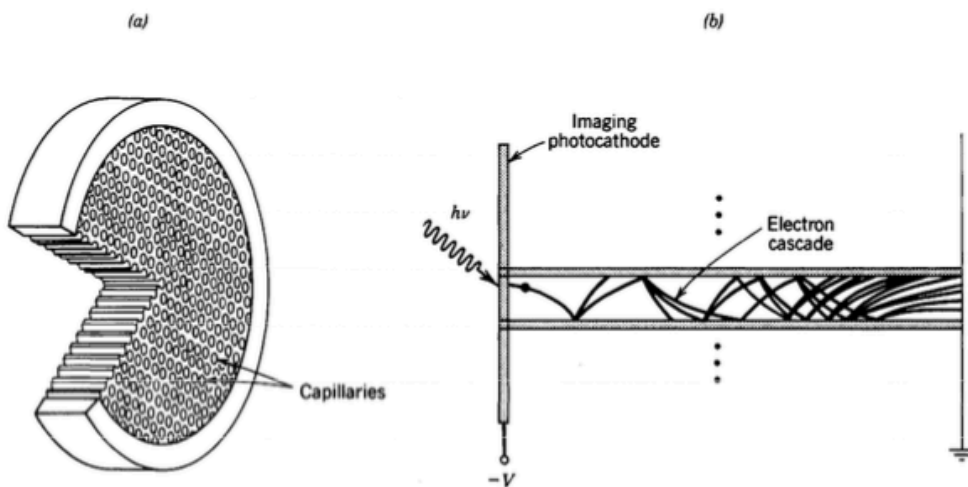


**Figure 2.9: Schematic and working principle of a micro channel plate detector (MCP); (a) A cut-away view of a micro-channel plate, (b) a single capillary in a micro-channel plate. Adapted from reference [67].**

The gain of an MCP device is limited by current and charge saturation, as well as ion feedback instability<sup>68</sup>, which occurs at high operating voltages. The positive secondary carriers are accelerated towards the front surface of the MCP and can produce secondary electrons if they have sufficient energy. This introduces noise to the system, and ions striking the capillary walls may also damage the channel.

### 2.1.7.2 PMT

The photomultiplier tube (PMT) is typically constructed with a photocathode, several dynodes and an anode within an evacuated glass housing<sup>69</sup>. The first PMT was invented in 1934 as a sensitive, low noise, fast light detector. Since then, they have been used expansively in nuclear and particle physics instruments, astronomy and medical diagnostic devices. They have been perfected since their invention, at close to their theoretical maximum of 43 % quantum efficiency at 350 nm<sup>70</sup> (quantum efficiency – the ratio of the generated carriers to the incident carriers). The dynodes in a PMT serve as electrodes where secondary electron emission can take place (see Figure 2.10). The electric field between the dynodes is controlled (each successive dynode at a slightly higher potential) so that the electrons emitted from the previous dynode strike the next with energies of a few hundred eV. This gives an exponential increase in electron multiplication. Research has found new dynode coatings to increase SEY and therefore reduce size and number of dynodes required<sup>71</sup>. Two geometries of dynodes are used – reflection and transmission – the most common of which is reflection, shown in Figure 2.10.

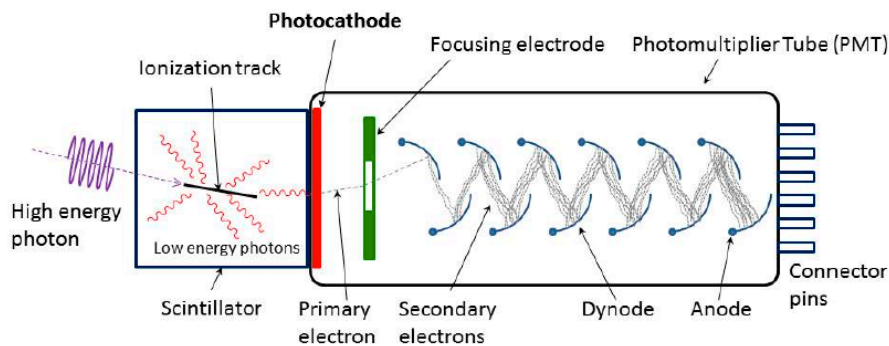


**Figure 2.10: Working principle of the typical PMT, reproduced from reference [72]. A photon is converted into a lower-energetic electron at the photocathode, emitted into the vacuum and accelerated towards and focused onto the first dynode. Secondary electrons are generated and accelerated on to subsequent dynodes, resulting in an amplified electric signal at the anode.**

## 2.2 Dynodes

### 2.2.1 Introduction to Dynode

The dynode is the structure within a photomultiplier tube (PMT) that multiplies electrons and demonstrates secondary electron emission. A PMT is built of many dynodes in series; see Section 2.1.7.2 above for reference. A PMT can be built with one of two geometries; reflection mode or transmission mode. In transmission mode, primary electrons enter and secondary electrons exit through opposite sides of the film. With a high film thickness (anything over 100nm), an internal drift field is required to pull the electrons towards the exit surface. In reflection mode, the secondary electrons exit from the same surface that the primaries impact, and biasing occurs only between dynodes and not across them.

### 2.2.2 Reflection and Transmission: Dynode Macrostructure Within EM Device

Traditionally, reflection secondary electron emission (RSEE) was used for electron multiplication devices. The use of transmission secondary electron emission (TSEE) for electron multiplication devices was proposed by Lubszynski<sup>73</sup>, McGee<sup>74</sup> and Sternglass<sup>75</sup> in the mid-60s. RSEE gave short dynode lifetimes towards the last few gain stages in a PMT due to the higher average currents one must be able to handle. TSEE was expected

to reduce radiation damage caused by highly energetic electron bombardment, as electrons lose kinetic energy on traversing the film dynode, as well as producing secondary electrons with a much lower energy. Another important advantage is the reduction of surface-termination that TSEE gives; the often very fragile surface terminations – which give the valuable negative electron affinity – would not be bombarded by highly energetic incoming electrons, but by the lower energy secondary electrons. Other advantages of dynodes using TSEE include; (1) improvement in quantum detection efficiency and pulse amplitude fluctuations; (2) a reduction in transit-time-through-device fluctuations; (3) uniform response over the area of the dynode, eliminating transit-time differences caused by angles of dynodes within the structure (see Figure 2.11); and (4) short total transit-time and dead-time<sup>76</sup>. The maximum SEY as a function of primary electron energy increases with TSEE at over 25 keV, as shown by Shih *et al.* in “Secondary Electron Emission Studies”, as opposed to their 1 keV for RSEE. This is because electron escape depth is fairly irrelevant in TSEE, and therefore the transmission dynode can be optimised by size for specific incident electron beam energy.

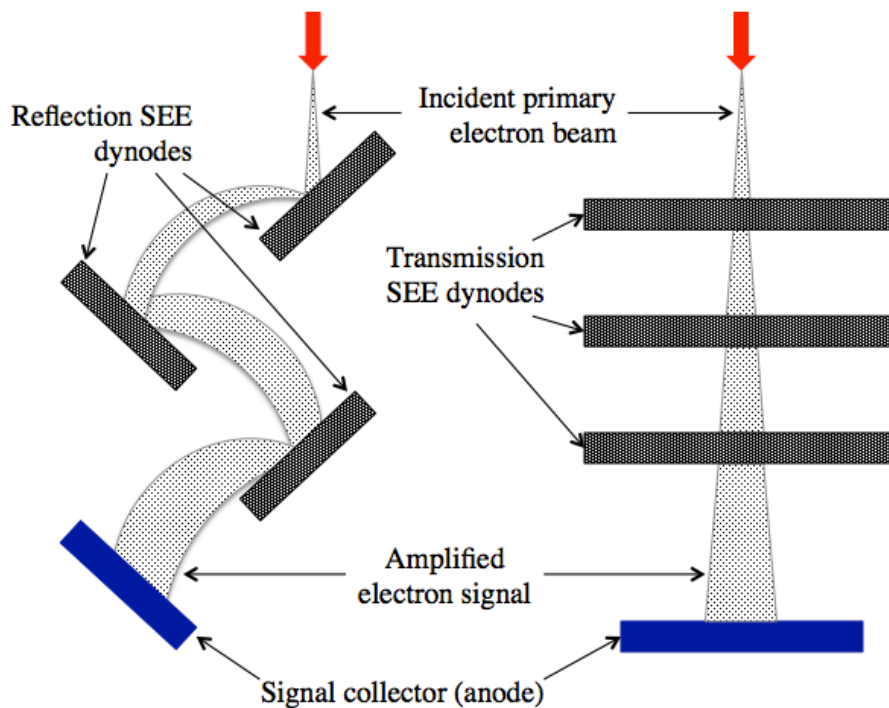


Figure 2.11: Schematic showing electron multiplication through three stages in the two different modes – reflection (left) and transmission (right).

In summary, the transmission dynode is superior, as linear propagation of electrons through the electron multiplication device gives minimum spread of kinetic energies of electrons, guaranteed primary collision at the first dynode, and freedom from beam contamination effects which degrade the NEA surface.

For transmission dynodes to be effective, it is necessary to use very thin films, in the order of microns, of high-purity single-crystal diamond, along with an internal field to accelerate the electrons through the film<sup>77</sup>. Successful development of such a device would provide previously unattainable emission performance. This study attempts to produce such a device using polycrystalline diamond up to 50  $\mu\text{m}$  thick.

### 2.2.3 Materials used for bulk material/central layer

Development into suitable materials for dynodes in photomultipliers started in the early 1930s. Insulating materials were found to have high SEY, and were successfully used in commercial devices based on the RSEE geometry. Research into materials for transmission SEE started about 30 years later, and most of the research can be separated into three different classes of materials aimed at developing different applications. In the 50s and 60s, bulk KCl was the material of choice for use in transmission dynodes for high-speed electron multiplication. In 1962, the low density KCl dynode (consisting of an AlO layer supporting a thin Al/Au layer and low density KCl) brought significant increase in SEY with an applied external collecting voltage. Bulk CsI activated by Cs came about in 1972 increasing transmission SEY (TSEY), followed by semiconductors with NEA; GaAs and Si, in the 1970s. Diamond has been studied since the 1990s for use in electron multiplication devices, and has shown many advantages compared to the previously used materials (Section 2.3).

Research into SEE by diamond film has mainly been of the reflection geometry, with only a few papers reporting on the transmission properties of diamond<sup>78,79,80,81</sup>. This is due mainly to the technical challenges in fabrication of such thin diamond films. The latest development in research for novel transmission dynode materials is the MEMBrane project<sup>82</sup>, where MEMS and ALD technologies are used to fabricate membranes on the order of 10 nm, from SiN, Al<sub>2</sub>O<sub>3</sub> and MgO compounds. These films have shown great potential for transmission SEY at low primary electron energies.

### 2.2.4 Electronic Contacts

It is important to consider the electrical contact between different layers within a dynode and to the external circuitry; these can be dependent on the type of bonding across the interface due to the molecules present, as well as the method for producing that interface.

An ohmic contact is a non-rectifying electrical junction; a junction which has a linear current-voltage relation as following Ohm's Law. These are used to allow charge to flow between the two materials, usually both conductors, without excess power dissipation or loss of signal due to voltage thresholds. The term 'ohmic contact' generally refers to the interface between a metal and a semiconductor. Low-resistance, stable ohmic contacts are critical to the efficient performance of semiconductor devices, and require effort to achieve. Poorly prepared contacts can easily show non-ohmic rectifying behaviour, by inducing a depletion region within the semiconductor near the junction, and blocking the flow of charge out of the device to the external circuitry. Ohmic contacts are typically constructed by depositing specially selected thin metal films onto the semiconductor surface<sup>83</sup>.

Junctions such as p-n junctions and Schottky barriers do not demonstrate linear ohmic behaviour. A Schottky barrier is a potential energy barrier which allows current to pass in one direction but impedes it in the other, suitable for use as a diode. If a Schottky barrier is low enough, it assimilates an ohmic contact. The Schottky barrier height depends on the combination of metal and semiconductor energy levels<sup>84</sup>. In practice, the molecular bonding at the interface induces gap states, and surface pinning of the centre of the band gap to the Fermi level<sup>85</sup>. This challenges the formation of ohmic contacts in semiconductors such as Si and GaAs, and lowers device performance.

With dynodes, careful selection of conductive layer materials is required as it is important to preserve as much primary electron energy as possibly by avoiding electron-electron scattering. Because of this, metals are not well suited, since, for

example, a 1 keV primary electron loses the majority of its energy passing through a 2 nm thick layer of Au. TiN and graphene have been explored in the MEMbrane project (Section 2.2.3), with TiN preferred. This is most likely due to its similar properties to the 'transparent' conducting oxides (TCOs). They have large band gaps and are transparent, but remain conductive for good carrier mobility. TCOs are commonly semiconductors compound with oxygen. ITO and non-expensive Al-doped ZnO could also be suitable for the use of the conductive layer for transmission dynodes<sup>86</sup>.

Boron-doped diamond (BDD) is a conductive material that could be successful in providing the electrical contact for diamond film dynodes. It would produce a homojunction, with the difference in doping level causing band bending and induction of a depletion region.

## 2.3 Diamond

Despite recent advances in solid-state electron multipliers using gain mechanisms such as the avalanche photodiode, the performance of vacuum-tube amplifiers remains unequalled. The choice of dynode material for these devices is crucial to creating the best devices yet. Synthetically deposited CVD diamond offers significant advantages over other materials. Diamond has a very high SEY, up to 132 at a primary electron energy of 2.8 keV<sup>87</sup>.

A high dynode SEY brings several benefits to electron multipliers. First, it decreases the number of gain stages required to reach the required signal level. This also means that it decreases the response time of the electron multiplier and reduces noise<sup>88</sup>, as with fewer steps, there will be a smaller range of times for the electrons to traverse the device. Lower number of required dynodes provides an advantage in terms of device size, cost and complexity.

Diamond's wide band gap of 5.45 eV<sup>89</sup> prevents low energy secondary electrons from losing energy through electron-electron collisions – giving a large escape depth and a large secondary electron yield. Diamond's large band gap removes thermal noise at room temperature, and lower noise at higher temperatures compared to other conventional devices. Finally, diamond offers significant advantages due to its high radiation hardness, meaning device lifetime will be longer compared to other materials. Diamond also offers doping possibilities, providing the conductivity required for continuous SEE.

### 2.3.1 Diamond Structure

In nature, elemental carbon has a few naturally forming arrangements of atoms, with the most common being graphite and diamond structures. Graphite is the thermodynamically stable allotrope of carbon at room temperature and pressure (see Figure 2.15), with a layered, planar structure (see Figure 2.12). The carbon atoms in graphene layers are arranged in a honeycomb lattice where each carbon atom is covalently bonded to three others (*sp*<sup>2</sup> hybridized), with weak Van der Waal forces governing inter-layer bonding. This allows layers of graphite to be easily separated or slide past each other. Diamond, on the other hand, is formed at high temperature and pressure in the Earth's mantle, and the growth occurs over periods from 1 billion to 3.3 billion years. This means that all of the diamonds we will mine naturally have already been formed; imposing a limit on supply, not forgoing that mining requires many difficult conditions.

Diamond's carbon atoms are each covalently bonded in a tetrahedral structure to four other carbon atoms ( $sp^3$  hybridized), in a metastable allotrope, arranged in a variation of the face-centred cubic crystal structure called a diamond lattice (see Figure 2.13). Figure 2.13 (b) shows the arrangement of carbon atoms in the diamond unit cell, consisting of a face-centred cubic lattice structure with a lattice constant  $a_0 = 0.357 \text{ nm}^0$ . The minimum distance between neighbouring atoms is  $\sqrt{3/4} a_0$ , although this value is dependent on temperature and impurity concentration.

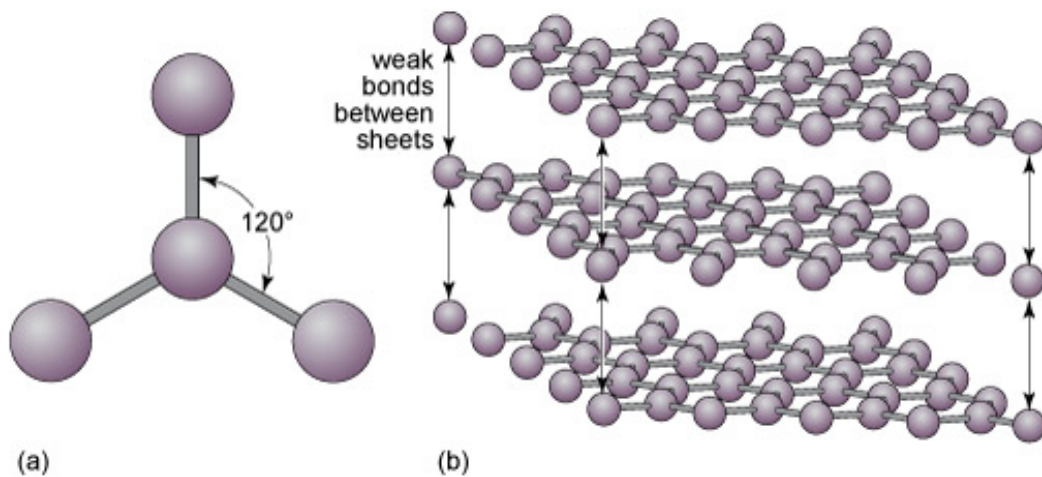


**Figure 2.12 The graphite structure: (a) triangular arrangement of covalent bonds around a carbon atom in the same plane; (b) part of the 3D structure of graphite, showing strongly bonded hexagonal sheets of carbon atoms, connected by weak van der Waals bonds, reproduced from reference [91].**

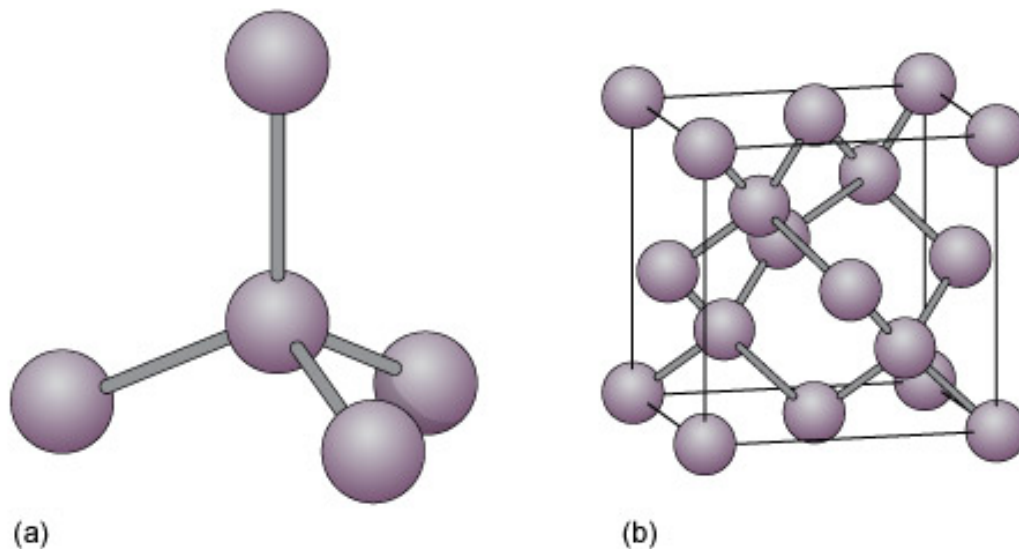


**Figure 2.13: The diamond structure: (a) tetrahedral arrangement of covalent bonds around a carbon atom; (b) unit cell showing a tetrahedral structure (face centred cubic lattice structure), reproduced from reference [92].**

Diamond owes its extreme hardness as well as other principle properties (shown in Table 2-2) to this tetrahedral arrangement of strong covalent carbon-carbon single bonds. This allows diamond to be used as thin film diamond (few hundred microns) without being too fragile. However, for the application of transmissive dynodes the films need to be much thinner, in the order of 1-10s of microns. At this point polycrystalline diamond films are fragile (must be handled with utmost care).

Diamond can be doped to form a semiconducting material with elements such as boron, nitrogen, silicon, phosphorous, nickel, lithium, sodium and sulfur<sup>93,94,95,96</sup>. However, the process of doping is difficult due to its extremely compact and rigid lattice, with little space for these substitution impurities.

Diamond possesses excellent electron emission characteristics. It has a wide band gap of 5.45 eV and negative electron affinity (see Section 2.1.4.1). Diamond's high thermal conductivity, which is roughly five times as high as copper<sup>97</sup> ( $4.01 \text{ W cm}^{-1} \text{ K}^{-1}$ ), is unusual for electric insulators due to its strong covalent bonding and minimal phonon scattering. This allows fast heat dissipation when thin films are bombarded with a high-energy electron beam, allowing for continuous device operation.

Diamond's high dielectric strength can tolerate much stronger electric fields before breakdown, allowing a larger bias to be applied across the thin film to accelerate the carriers towards the surface of the material and stimulate transmission.

**Table 2-2: Some of the principle properties of diamond, reproduced from reference [98].**

Property	Value	Units
Hardness	$1.0 \times 10^4$	$\text{Kg mm}^{-2}$
Young's modulus	1.22	GPa
Strength, tensile	>1.2	GPa
Strength, compressive	>110	GPa
Thermal expansion coefficient	$1.1 \times 10^6$	$\text{K}^{-1}$
Thermal conductivity	20.0	$\text{W cm}^{-1} \text{ K}^{-1}$
Optical index of refraction (at 591 nm)	2.41	n/a
Optical transmissivity (from nm to far IR)	225	n/a
Electron mobility	2200	$\text{cm}^2 \text{ V}^{-1} \text{ s}^{-1}$
Hole mobility	1600	$\text{cm}^2 \text{ V}^{-1} \text{ s}^{-1}$
Dielectric Strength	$1.0 \times 10^7$	$\text{V cm}^{-1}$
Work function	Negative	n/a
Band gap	5.45	eV
Resistivity	$10^{13} - 10^{16}$	$\Omega \text{ cm}$

### 2.3.2 CVD Diamond For Dynode Applications

#### 2.3.2.1 Defects / Traps

It is very difficult to synthesise CVD diamond film without small concentrations of N impurities. This is because nitrogen is difficult to exclude from a growth system. Besides, its presence has catalytic influence on diamond nucleation and growth, with films grown with N showing a considerably improved crystalline quality compared to those without<sup>99</sup>. Nitrogen impurities introduce deep traps within the structure that can decrease electron drift paths and impede electron migration through the device. CVD diamond films can contain a substantial number of structural defects, which create additional energy bands within the band gap of diamond and therefore contribute to electron emission at low electric fields<sup>100</sup>.

A drop in charge collection efficiency (CCE) can be observed as the intensity of the Nitrogen vacancy centre (NV) (quantified from integrated fluorescence intensity)

decreases<sup>101</sup>, see Figure 2.14. Lattice defects and dislocations are also known to deteriorate CCE by trapping charge carriers and reducing their lifetimes<sup>102</sup>.

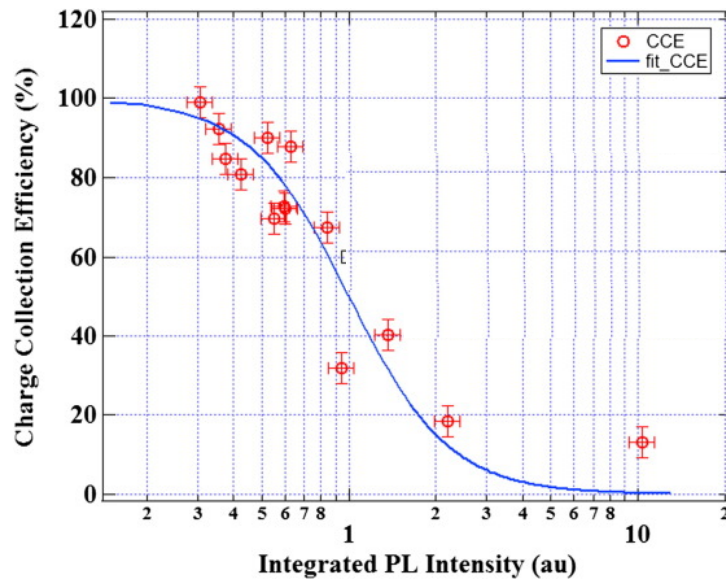


Figure 2.14: Plot of charge collection efficiency (CCE) of integrated NV phonon sideband. Solid line is fitted to describe the rapid decay of CCE with  $I_{NV}$ . Although,  $I_{NV}$  is expressed in arbitrary units, it provides a good representation of the total amount of impurity present in relation to the CCE of the CVD diamond bulk. It implies that the CCE decays rapidly with  $I_{NV}$ . The rate of decay is 2.5. The error bars along the x-axis of roughly 10% shown were attributed to both the system noise and measured intensity fluctuations at 12 different positions in the sample. The error bars along the y-axis are estimated from the standard deviation ( $\pm 3\sigma$ ) of the three separate CCE measurements under the same bias conditions. Figure and caption reproduced from reference [103].

### 2.3.3 Diamond Quality

Synthetic CVD of diamond films produces films of different qualities, such as single-crystal (sc) and polycrystalline (pc) class of different sizes (micro-, nano-, ultranano-), where sc- is the highest quality structure, with lowest  $sp^2$  (graphite) content and no grain boundaries and minimum defects. Depending on the desired properties of the film, it is possible to synthesise films with specific surface morphologies, roughness, and surface-conductivity, amongst other properties.

The crystal morphologies of CVD diamond films depend on the process parameters used for synthesis, particularly the gas phase mixture. For  $CH_4/H_2$  gas compositions, with ratios up to 2 % methane in hydrogen, micro-polycrystalline morphologies are deposited. This class usually has a linear dependence of surface-roughness on film thickness, which can be a hindrance with certain applications when film thicknesses on the order of a few microns are used. This class also contains relatively low carbon  $sp^2$  content, which is concentrated at the crystal grain boundaries.

Nano-polycrystalline morphologies generally occur when a greater than 3 % ratio of methane in hydrogen is used for the gas mixture. They contain a greater content of carbon  $sp^2$  than the micro-pc films, with more grain boundaries and lower surface-roughness ca. 10-20 nm (rms), with grain sizes ca. 10-500 nm.

It is important to note that for polycrystalline diamond film dynodes, transportation and emission of low-energy electrons is very efficient regardless of crystal orientation. However, the emitted energy distribution and SEY varies with this and surface

properties such as structure and termination. Transmission SEY of pc- diamond samples was lower than with sc-, attributable to increased electron scattering at grain boundaries<sup>104</sup>. Diffusion lengths were also found to be much larger in sc- (8.1  $\mu\text{m}$ ) as opposed to pc-diamond films (1.3  $\mu\text{m}$ ). For two films of similar thickness but differing crystal morphologies, sc-morphology gives a greater transmission SEY. However, pc-diamond is widely available, relatively inexpensive and can be deposited over large areas, making the manufacture of pc-diamond dynode devices practical.

It is speculative to suggest that due to the polycrystalline nature of the CVD diamond films that it is possible to synthesise in the laboratory, the films could act similarly to the micro-channel plate multiplier (see Section 2.1.7.1). This is due to the linear growth of diamond single crystals shown here. Electrons will most likely be lost once impacting with the crystal boundaries, keeping multiplication within each crystal. This could give rise to a spatially resolved diamond electron multiplier if coupled with an electrode layer.

## 2.4 Diamond Growth Techniques

To briefly explain chemical vapour deposition of diamond, as you've already heard it today. It is when you have a hot gas mixture, predominantly Hydrogen, and a small percentage of methane, activated by either thermal or MW methods, above a substrate where you want to grow it. The activation of the gas forms radicals of methane which begin to deposit onto the substrate, slowly building up the diamond structure. Hydrogen acts to etch away any  $\text{sp}^2$  carbon (which forms graphite) in favour of  $\text{sp}^3$  (which forms diamond).

Very early on in industrial human development, in 2000 BC, diamond was used by the Chinese as an industrial material owing to its extreme hardness. However, natural diamond was a limited material due to its rarity and high cost, and therefore it was not used in science and engineering until the last century, despite its exceptional properties. Under standard conditions, graphite is the thermodynamically stable allotrope of carbon (see Figure 2.15), whilst diamond exists as a metastable phase of carbon. Therefore, synthetic production of diamond is required to field enough diamond for industrial applications. This barrier, provided by the expense and scarcity of natural diamond, was the driving force behind the development of synthetic diamond growth techniques.

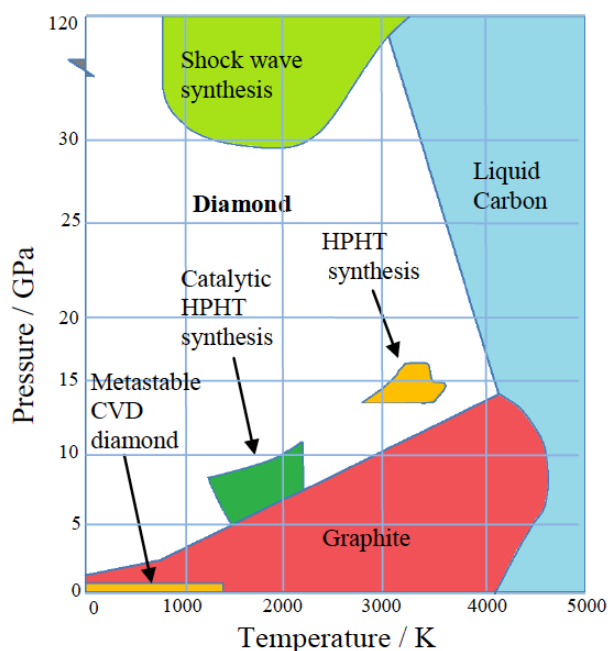


Figure 2.15: Phase diagram of pressure against temperature for elemental carbon, reproduced from reference [105].

Over fifty years have passed since a method was first described for the pyrolysis of hydrocarbons to form thin film diamond. Initially, diamond growth was only possible using diamond substrates, however, since then, the method has been refined and adapted, to the extent that diamond can now be deposited onto a variety of different substrate materials, with almost single crystal structure, with a chemical purity exceeding that of natural diamond.

#### 2.4.1 HPHT

Thermodynamically, the conversion Gibbs free energy of graphite to diamond is shown by a small, positive value<sup>106</sup>:

##### Equation 2.3



This endorses diamond as a meta-stable form of carbon. The rate of diamond to graphite conversion is incredibly slow, and increasing the temperature increases this rate, as is true for most reactions. The rate becomes observable above 1200 °C, at 1 atm, showing that diamond is less stable at higher temperatures. In order to bring the Gibbs free energy of conversion of graphite to diamond into the negative spontaneous region, it is necessary to apply pressure, as can be seen in Figure 2.16. Diamond is the stable carbon allotrope above the line, graphite below.

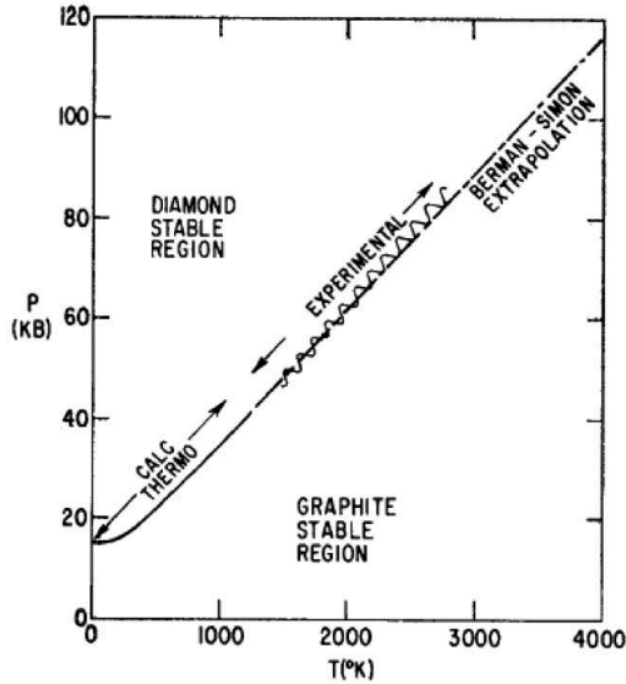


Figure 2.16: The graphite-diamond equilibrium curve, taken from reference [107]. Reproduced from Copyright 1962, The American Chemical Society.

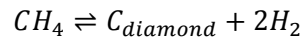
After many attempts at and undetermined reports of laboratory synthesis of diamond, the General Electric Company carried out the first reproducible experiment in 1955. It used a high-pressure, high-temperature (HPHT) method assimilating the conditions of the natural formation of diamond in the Earth's mantle. Their experiment mixed graphite and a catalyst transition metal, usually Ni, Fe or Co, and then exposed the mixture to pressures of 80 – 300 kbar and temperatures of 1900 – 3000 °C. Currently, this method is used for industrial purposes, and unless a catalyst is used, HPHT diamond crystals grow only to very small sizes. Both nickel and cobalt can be found as impurities in the synthetic diamonds, hence the crystals are often coloured yellow and therefore unsuitable for use in the jewellery industry, but are still used in cutting tools and as abrasives. One limitation of the HPHT process is the slow growth rate, which restricts the crystal size to about 1 cm<sup>3</sup><sup>108</sup>.

To enable conceivable use of diamond applications it was necessary to find a process which would allow formation of diamond in functional forms such as thin films to be producible at lower costs.

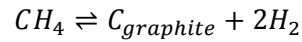
#### 2.4.2 CVD

A far more popular process in the research industry is chemical vapour deposition (CVD), where diamond films are grown from a hydrogen and hydrocarbon gas mixture onto a substrate surface. This can be realised by adding one carbon atom at a time to an initial lattice template, to result in a tetrahedrally bonded carbon system – diamond. This technique can feasibly be achieved at lower pressures than the HPHT technique, which provides advantages in terms of equipment and costs<sup>109</sup>. Eversole used this concept in 1958<sup>110</sup>, in which thermal decomposition of carbon-containing gases was used to grow diamond on natural diamond crystals, at 900-1100 °C, at two different pressure ranges. Eversole's lower pressure reaction, at pressures below atmospheric, is performed starting with a methyl group-containing gas:

Equation 2.4



Equation 2.5



The early experiments had very low growth rates, with a substantial improvement on Eversole a decade later of a linear rate of up to  $250 \text{ } \mu\text{m h}^{-1}$ <sup>111</sup>. In the same year<sup>112</sup>, another development reported atomic hydrogen present in the gas phase during the growth process favorably etched graphite (sp<sup>2</sup>) over diamond (sp<sup>3</sup>)<sup>113</sup>. This crucial discovery made synthetic diamond growth by CVD a possibility in the commercial market.

It is generally accepted that atomic hydrogen is very important to the CVD process. Its primary function is to terminate the waiting carbon bonds at the surface of the diamond layer, whilst hydrogen atoms are also used to create reactive radicals such as CH<sub>2</sub> by cleaving neutral hydrocarbons; these radicals bond to the exposed carbon and form trigonal sp<sup>2</sup> (graphite) or tetrahedral sp<sup>3</sup> (diamond) bonded carbon<sup>114</sup>. The preferential etching of graphite over diamond is due to the etch rate of sp<sup>2</sup> bonded carbon being much higher than of the sp<sup>3</sup> carbon; hydrogen also suppresses the build up of polymers or large ring structures which are unconstructive for diamond film growth<sup>115</sup>.

CVD processes require consistently followed procedures, such as substrate selection, substrate preparation and the temperature range; since Eversole showed insufficient diamond growth takes place at lower temperatures and excessive graphite deposits at higher temperatures. Current practices use molybdenum, silicon nitride and tungsten carbide as substrates, and pretreatment is required to provide areas of nucleation for diamond growth. Current publications show pretreatments of mechanical polishing by diamond powder or through ultrasonic bathing in a mixture of abrasive grit.

Bachmann *et al.*<sup>116</sup> were the first to demonstrate that synthetic diamond growth is only possible within a small area on the C/H/O gas phase diagram, shown in Figure 2.17.

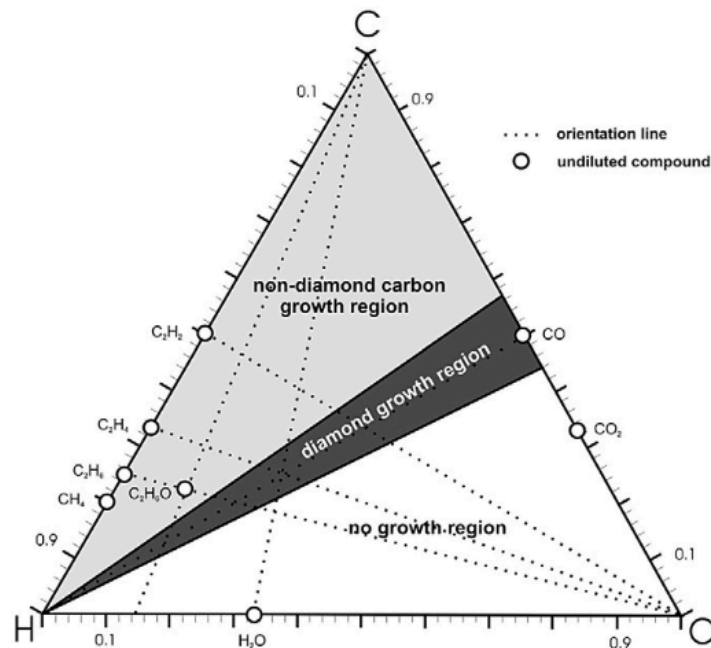


Figure 2.17: C-H-O phase diagram for diamond growth, reproduced from reference [117].

CVD comprises of many complex chemical reactions occurring in the gas phase above a substrate surface. A source of activation is required to initiate the deposition, which can be achieved by thermal processes as in the case of hot-filament CVD (HF-CVD) systems<sup>118</sup>. Another method used is microwave- (MW-) activated plasmas, which use similar process conditions to HF-CVD but offer advantages such as higher growth rates. Unfortunately, this also causes MW plasma reactors to be a significantly more expensive method.

#### 2.4.2.1 Chemical Reactions in the CVD Reactor

Molecular hydrogen in the gas phase dissociates into atomic hydrogen<sup>119</sup>, after which a complex series of reactions takes place between these hydrogen atoms and hydrocarbon species (initiated from methane), as well as between the hydrocarbon species. The mixed gas phase then enters the activation area in the chamber, which heats the gas to high temperatures of the order of 1-2 thousand degrees Celsius, which causes the molecules to dissociate into reactive radicals. These reactive species take the form of atoms, ions and electrons and continue mixing, experiencing a complicated chain of reactions until they come into contact with the surface of the deposition substrate. Once on the diamond surface, a general growth model as shown in Figure 2.18 occurs. Atomic hydrogen removes an H from a dangling C-H surface bond to form H<sub>2</sub>, leaving a surface C radical. Various hydrocarbon radicals in the gas phase can adsorb onto this site, of which the main growth mechanism is the addition of CH<sub>3</sub> radicals<sup>120</sup>. A frequent occurrence is the recombination of the active surface site with a hydrogen atom<sup>121</sup>, meaning that the process is a slow one; many competing steps forward and back.

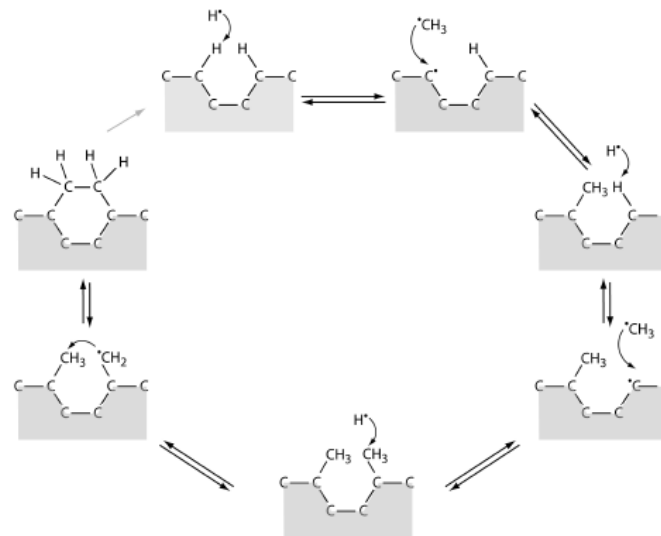


Figure 2.18: A schematic showing the simplified standard CVD diamond (111) growth model. Adapted from references<sup>122,123,124</sup>, reproduced from reference [125]. The growth mechanism begins with the removal of a dangling H atom, leaving a reactive surface site.

#### 2.4.2.2 HF-CVD

In 1982, a hot filament reactor was built which grew high quality diamond films on non-diamond substrates<sup>126</sup>. This process operated using 0.5 – 2.0 % CH<sub>4</sub> in H<sub>2</sub>, a total flow rate of 4 – 200 cm<sup>3</sup> min<sup>-1</sup>, at pressures from 0.5 up to several tens of Torr, achieving significant growth rates of ~ 1 μm h<sup>-1</sup>. Tungsten filament was used at about 2000 °C, heated by a D.C. source, to accelerate the diamond deposition process. The substrate was kept in the lower temperature range of 600 – 1000 °C, as too high a temperature is

preferential to deposition of graphite structures (see Section 2.4.2). Materials used for the substrates were silicon, molybdenum and silica glass plates, with no significant difference in surface morphologies and geometries between substrate materials.

Currently, HF-activation of the hydrocarbon-hydrogen gas mixture is a well-established process<sup>127,128</sup> to grow diamond at low pressures. It is simple and cost effective, and runs at lower temperatures relative to plasma processes. The growth rates are also low ( $\sim 1 - 10 \text{ } \mu\text{m h}^{-1}$ ) compared to those of plasma activation. An advantage to HF-CVD is the possibility of scale up to deposit diamond on much larger areas and unrestricted shapes, restricted only by the reactor chamber dimensions<sup>129</sup>.

Another variable to consider is the material of the filament, with tungsten, tantalum or rhenium mainly used. Tungsten and tantalum are advantageous in their low cost; however, they react with the carbon to form brittle carbide layers, limiting their lifetime. The stability of the process is therefore reliant on the filament. It is also important to note that metal impurities will be present in the diamond film due to contamination by the filament<sup>130</sup>.

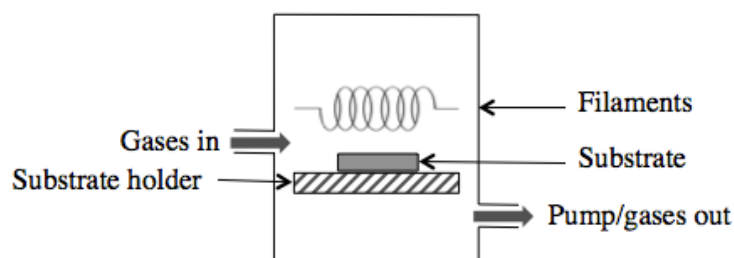


Figure 2.19: Schematic representation of two types of low pressure CVD reactor, created with reference to [131].

#### 2.4.2.3 MW-Plasma CVD

In 1993, the microwave plasma (MW-plasma) reactor<sup>132,133</sup> was used to activate the gas mixture instead of the hot filament, with similar synthesis conditions to those previously reported. However, this method gives a growth rate of  $\sim 3 \text{ } \mu\text{m h}^{-1}$ , a significant improvement on previous methods. Note that the conditions used here are well within the graphite region of stability on the pressure vs. temperature phase diagram of elemental carbon (see Figure 2.15). This ability to synthesise diamond under ambient pressure is the fundamental advantage of CVD methods for feasible diamond growth, in comparison to HPHT methods.

Since then, many methods of diamond growth have been developed, with the main differences arising in the method of activation of the gas-phase carbon-containing molecules. The many different methods will not be discussed here as they are outside of the scope of this project/thesis. The most commonly adopted type of MW-plasma CVD reactor is the linear antenna type (see Figure 3.4), with excitation frequency of 2.45 GHz<sup>134</sup>.

#### 2.4.2.4 Boron Doping

CVD diamond can be deposited with boron incorporated into its lattice. This increases the conductivity of diamond, as boron is a trivalent atom (3 outer electrons), and thus introduces a shallow acceptor level into the band gap at 0.37 eV above the band gap, producing an extrinsic p-type semiconductor. At boron concentrations in the range of  $10^{19} - 10^{21} \text{ cm}^{-3}$ , conduction occurs by nearest-neighbour and hopping of holes between

ionised B sites<sup>135</sup>, with a drop in mobility<sup>136</sup>. Towards the higher concentrations, interaction of boron centres leads to an impurity band that moves closer to the valence band maximum as the impurity concentration increases<sup>137</sup>. For sufficiently high boron concentrations, the diamond can tend to a metallic conductivity, exhibiting a resistance of  $10^{-3} \Omega$  at room temperature with a boron concentration of  $10^{21} \text{ cm}^{-3}$ <sup>138</sup>. It is important to consider the effect of boron incorporation into the lattice, in terms of stresses on the system, due to the difference in radius of the C and B atoms<sup>139,140</sup>.

$\text{B}_2\text{H}_6$  is the commonly used source of boron for boron incorporation into CVD diamond. Due to its high toxicity, this is usually diluted in solutions of  $\text{H}_2$  at low percentage levels. When this mixture is added to the CVD gas composition, a series of reactions form active radicals, of which B and  $\text{BH}_3$  are most abundant near the deposition surface<sup>141</sup>. These radicals join the hydrocarbon radicals in reaction with the surface radical sites (see Section 2.4.2.1), by a similar ring expansion mechanism, by insertion of B species into the C-C bond on the diamond surface<sup>142</sup>. Boron incorporation shows preference for (111) diamond facets<sup>143</sup>, and occupation of substitutional sites in the diamond lattice.

Boron-doped diamond (BDD) is itself used as a material with high SEE. The value of SEY of BDD depends inversely on the impurity level, as seen in Figure 2.20.

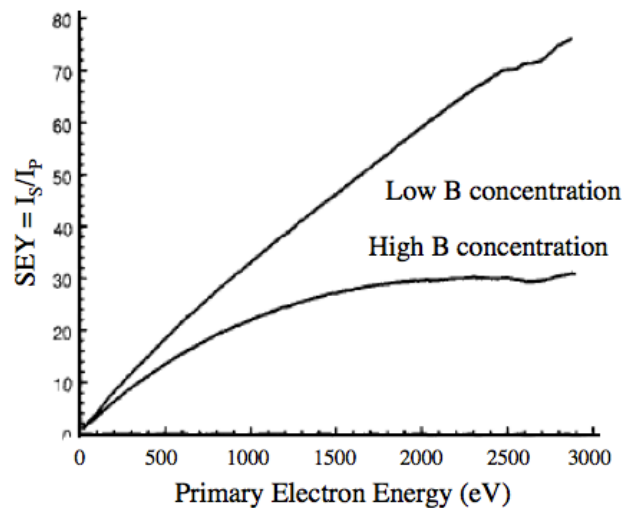


Figure 2.20: Effects of B-doping concentration on SEY. Reproduced from [144].

#### 2.4.2.4.1 Surface States

Doping of semiconductors induces band bending at surfaces. Doping with phosphorous induces strong upward band bending, for example, which reduces electron emission by introducing a barrier even in the presence of NEA<sup>145</sup>. Doping with boron induces downward band bending<sup>146</sup>.

## 3 Experimental Methods

### 3.1 Diamond Film Dynode

#### 3.1.1 Novel Structure

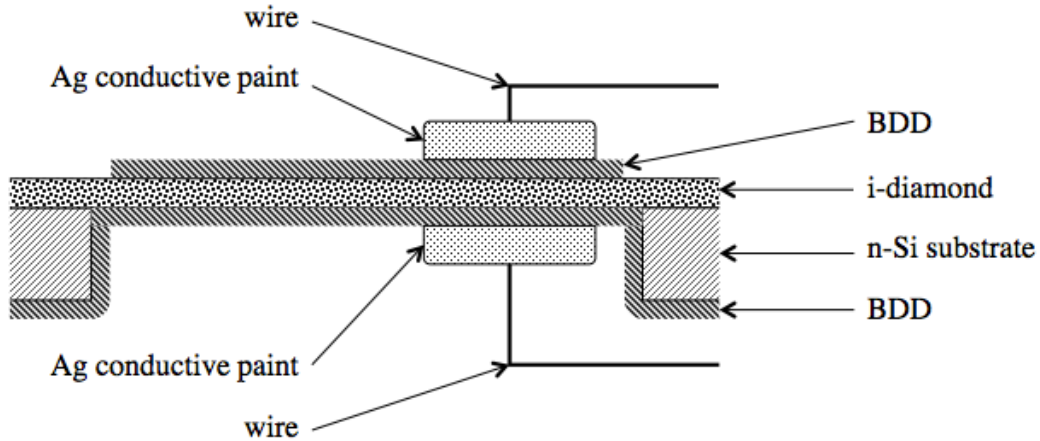


Figure 3.1: Schematic showing structural layers of novel diamond film dynode structure. Not to scale.

This project investigates a novel diamond thin film structure for transmissive dynode applications, as shown in Figure 3.1. The working dynode is of a semiconductor-intrinsic-semiconductor (SIS) geometry; a layer of undoped diamond (i-diamond) sandwiched between two much thinner boron-doped diamond (BDD) layers. The n-type Si was used as the initial deposition substrate, and then etched to expose free diamond layers in the centre, with remaining window frame-shape for support of the fragile substrate. Silver (Ag) conductive paint was used to connect wires for electrical characterisation of the samples.



Figure 3.2: Photograph showing sample; (left) Si window-frame side-up; (right) Growth-side (GS) of i-diamond layer up.

#### 3.1.1.1 Explanation of the Layers

The intrinsic diamond layer (i-diamond) provides the medium for secondary electron generation to occur. I-layers of different thicknesses were fabricated to observe secondary electron yield (SEY) versus thickness graphs; however, comparable results were not generated due to sample processing failures prior to testing (cracking, due to mishandling; and electrical shorting around the device). Boron-doped-diamond was deposited onto both sides of the i-layer to provide electrical contact for biasing of the i-layer. Its competing functions of; (1) being an electron source (due to high conductivity), as well as (2) being a material with high SEY that has similar lattice structure to the i-layer (at the thicknesses it was deposited at, ca. 2  $\mu\text{m}$ , there would have been no trouble

encouraging it to follow the lattice structure of the i-diamond), make it a very interesting structure for investigation. This work marks the first attempts at using a BDD/i-diamond/BDD SIS structure for SEE. BDD was used instead of its conductivity and the homojunction that would be conserved between the materials, and at the thicknesses involved, crystal lattice structure would be conserved at the i-diamond (111) type. The inclusion of the i-diamond layer instead of simply using BDD through the entire structure is due to the large depletion region induced by the i-diamond layer for increased electron/hole pair creation.

### 3.1.2 Fabrication of the Samples

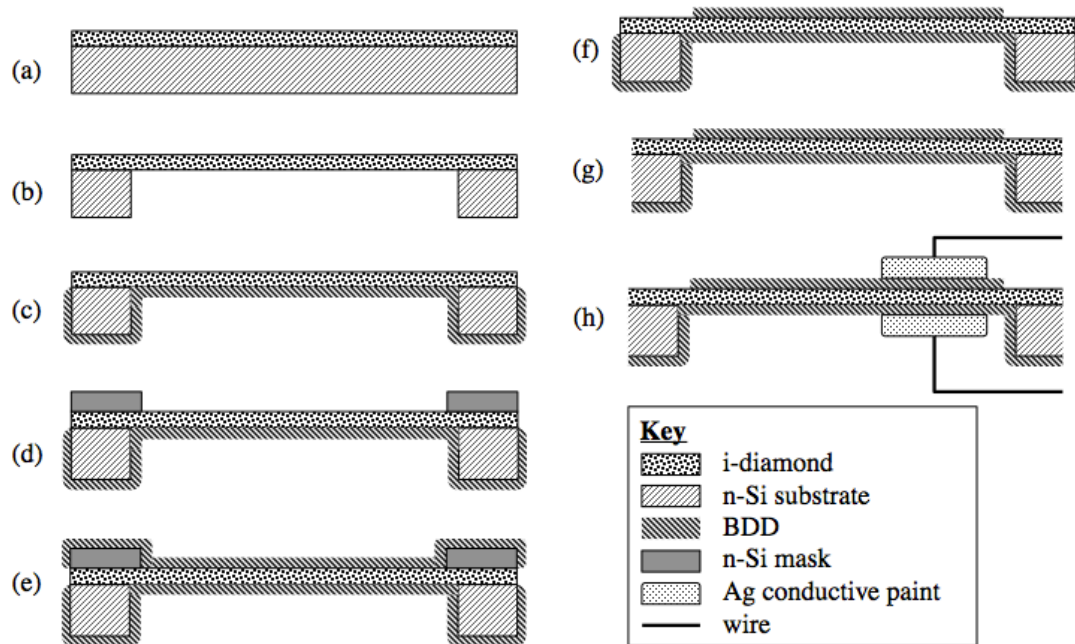


**Figure 3.3: Schematic showing sequence of fabrication steps. (a) i-diamond layer deposition on seeded n-Si substrate. (b) Removal of Si leaving window-frame support. (c) BDD layer deposition on seeded-side (SS) of i-diamond film. (d) placement of n-Si mask. (e) BDD layer deposition via n-Si mask on growth-side (GS) of i-diamond film. (f) Layer of BDD after removal of n-Si mask. (g) Laser etch of sides of sample to remove any conductive graphitic carbon, followed by boiling acid clean. (h) Electrical connection to BDD electrodes of wires via silver (Ag) conductive paint.**

Figure 3.3 shows the processes used to fabricate the novel diamond film dynode structure. Each process is described in full below. Initially, the Si substrate was removed completely to leave a freestanding diamond film. This resulted in all samples cracking at some point throughout the fabrication process, at which point the Si-window frame design was introduced for the last four samples. At every step past removal of Si (see Figure 3.3 (b)), special care was required to not put too much pressure or strain on the membrane. Filter paper was used to move the sample between processes, as tweezers required too much force. Multiple samples were produced, however, most of them were cracked by the time of testing. The cracked samples were however tested, as they still had the required active dynode structure characteristics.

About 90% of processed membranes did not survive the entire production process, demonstrating the great difficulty of using these pc-CVD structures for dynode applications, both in their manufacture and use.

### 3.1.2.1 Nucleation of Substrates

Prior to CVD diamond deposition, the n-type Si substrates were cleaned ultrasonically for 5 minutes each in acetone, methanol, ethanol, and finished in de-ionised water and blown dry with a nitrogen gun. These were then treated ultrasonically in a silane-salt solution for 10-15 minutes, rinsed in de-ionised water, and dried. Nano-cluster diamond suspension with an average particle size of 4-8 nm was prepared by sonication for 10 minutes to break up the clusters, before adding substrates to the solution for a further 5 minutes. The substrates were subsequently rinsed in de-ionised water and blown dry to be used in MW-CVD diamond deposition.

### 3.1.2.2 I-Diamond Layer Growth

The polycrystalline intrinsic-diamond films were deposited using microwave-plasma-assisted chemical vapour deposition (MW-CVD) (1.5 kW, 2.45 GHz, Seki-ASTeX microwave generator) on highly conducting n-Si (111) (0.5 mm thick by 10 mm<sup>2</sup> in area, seeded as described above (Section 3.1.2.1)). The films were deposited using a 4 % CH<sub>4</sub>/96 % H<sub>2</sub> source gas mixture for lengths of 2-7 hours. The flow rates were ~12.5 and 300 sccm, respectively. The microwave power and system pressure were maintained at 1200 W and 120 Torr, respectively. The substrate temperature was ca. 970 °C. The resulting film growth rate was ca. 4 μm h<sup>-1</sup>. The film's resulting resistance measured across the surface was > 500 MΩ. The film was hydrogen-terminated through diamond deposition process and by leaving it under pure 300 sccm H<sub>2</sub> flow at 30 Torr for time taken for plasma to cease at the end of the growth, ~1 min.

The reactor consisted of the mentioned generator coupled to the top of a cylindrical, water-cooled, stainless steel chamber. The microwaves create a resonant electromagnetic field pattern (mode), which is supported in the chamber, and the heated reactant gas mixture is excited to form a plasma ball. The visible edge of this plasma ball sits about 1 mm above the substrate, resting on a molybdenum substrate holder (see Figure 3.4).

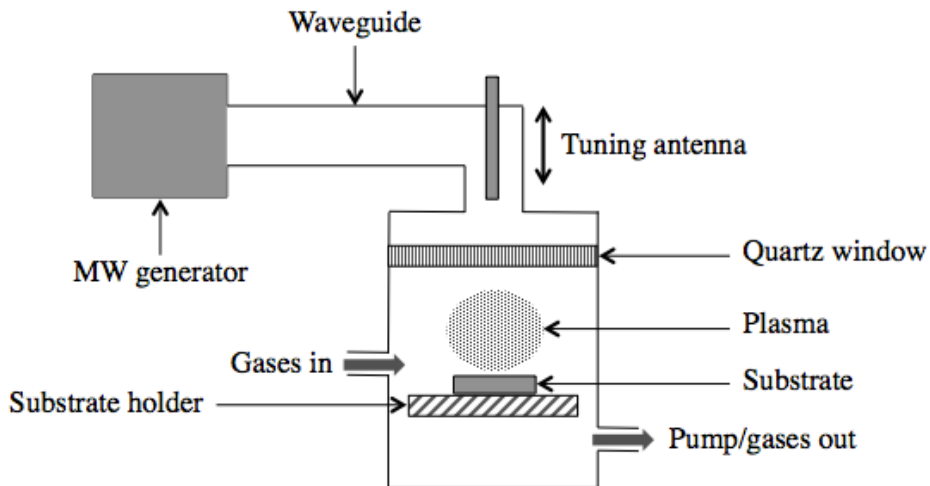
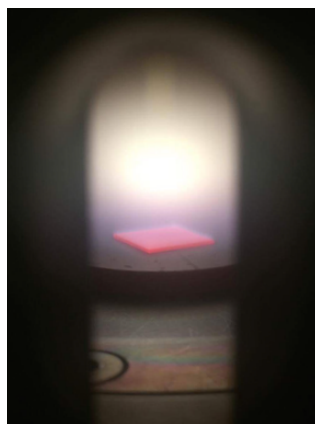


Figure 3.4: Schematic of a linear antenna-type MW-CVD reactor, created with reference to [147].



**Figure 3.5: Photo of MW-CVD diamond deposition. Si substrate is visibly hot-red, with plasma ball observable above it.**

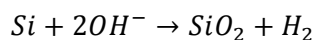
### **3.1.2.3 Laser Etch of Silicon Substrate**

The 10 x 10 samples of i-diamond layer deposited upon n-Si were etched through the Si side using a lab program on the laser micromachining set up (see Section 3.2.3). The program etched in rows horizontally, vertically, and then in both diagonal directions ( $y=x$ ,  $y=-x$ ). A square of side 7.2 mm was etched centred on the sample, at pitch 0.005 mm, laser speed  $2.5 \text{ mm s}^{-1}$  and pulse frequency 1000 Hz. This etched a depth of ca. 300  $\mu\text{m}$  into the 500  $\mu\text{m}$  Si substrate, and left a much rougher surface than prior to laser etching.

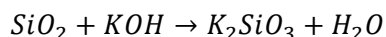
### **3.1.2.4 Wet Etch of Silicon Substrate**

After initial laser etching of the Si substrate, the substrate was treated in a KOH solution (8.57 g of KOH added to 20 ml of deionised water (30 wt.%) at  $70 \text{ }^\circ\text{C}$  for a period of 2 to 5 hours until Si is removed within the laser-etched square. This area is prone to attack from the  $\text{OH}^-$  anion at a faster rate and with far more nucleation sites as the laser treatment roughened the surface. Refer to equations (Equation 3.1, Equation 3.2) below for the reactions that occur within the solution. The molecules in solution do not attack the chemically inert diamond films.

#### **Equation 3.1**



#### **Equation 3.2**



### **3.1.2.5 Boron Doped Diamond (BDD) Layer Growth**

A hydrogen-terminated boron-doped diamond film was deposited on either side of the original i-diamond film using a homemade hot-filament CVD (HF-CVD) reactor, as shown in Figure 3.6. The i-diamond film on silicon substrate was placed 10 mm under three tantalum wires within a sealed chamber. A gas composition consisting of 200 sccm  $\text{H}_2$ , 0.1 sccm of 5 %  $\text{B}_2\text{H}_6$  in  $\text{H}_2$ , and 2 sccm  $\text{CH}_4$  – which is effectively 99.01 %  $\text{H}_2$ /0.99 %  $\text{CH}_4$ /0.0025%  $\text{B}_2\text{H}_6$  – flowed through the chamber, maintaining a pressure of 20 Torr. A current of 25 A was passed through the wires to heat them to ca.  $2000 \text{ }^\circ\text{C}$ , whilst the temperature at the sample was ca.  $850 \text{ }^\circ\text{C}$ . The reactor deposited boron-doped diamond for 1 hour, resulting in a film thickness of ca. 2-1  $\mu\text{m}$ . This gave a boron impurity

concentration of  $1 \times 10^{20} \text{ cm}^{-3}$ , which correlates to a film resistivity of  $\leq 0.01 \Omega \text{ cm}$ , according to the literature<sup>148</sup>.

Growing a layer of BDD on the seeded layer of i-diamond increases the quality of the crystals at this interface; the regrowth removes graphitic material and replaces it with  $\text{sp}^3$  carbon. This reduces grain boundaries and increases the crystal size.

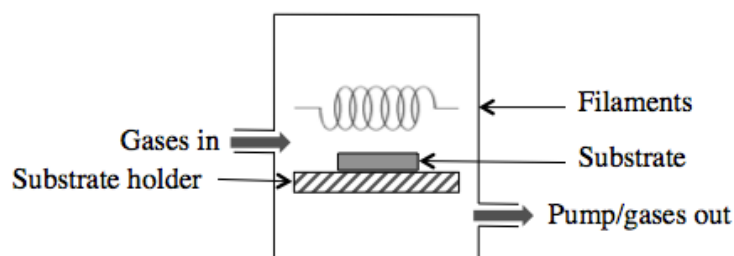


Figure 3.6: Schematic of a low-pressure HF-CVD reactor, created with reference to [149].



Figure 3.7: Photo of HF-CVD BDD deposition. Two substrates are visible under the glowing-hot tantalum filaments.

### 3.1.2.6 Boiling Acid Clean ( $\text{H}_2\text{SO}_4$ , $\text{KNO}_3$ )

Early testing suggested electrical shorting around the sample as opposed to electron movement through the device. This could be attributable to surface conduction (of contaminated surface H-species) or through BDD layer growth around the sides of the sample, giving electrical connection between the two theoretically separate BDD electrode layers. Prior to boiling acid clean, 0.3 mm off each side of the samples was removed by laser etch to aid in removal of electrical shorting along any possible graphitic substances or via BDD layer interfacing with the highly-doped n-Si. Samples were subsequently boiled in an acid mixture (100 mL  $\text{H}_2\text{SO}_4$  (95 % w/v) + 6.5 g  $\text{KNO}_3$ ) under reflux for 20 minutes, then left to cool and neutralised before being rinsed thoroughly in de-ionised water for several minutes.

This boiling acid treatment serves to O-terminate the sample surfaces (see Section 2.1.4.2), as well as to remove any adsorbed H-species or graphitic non-diamond carbon.

### 3.1.2.7 Electrical Contact For Testing Purposes

A drop of silver conductive paint (Ag dag) was deposited onto either side of the sample, and a stripped single wire was held in the liquid drop until the solvent evaporated. The connection between the sample and attached wire was annealed by heating on a hot

plate at 45 °C for 30 minutes. This formed a connection solid enough to support the system if held by the wires.

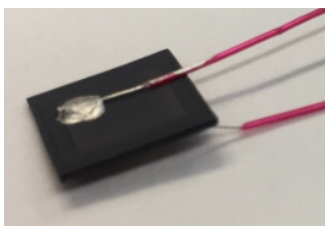


Figure 3.8: Photo of sample showing electrical connection via silver conductive paint.

## 3.2 Structural Characterisation Techniques and Equipment

### 3.2.1 Scanning Electron Microscopy

Scanning electron microscopy (SEM) is a surface characterisation technique that produces images of a sample by scanning it with a focused beam of electrons. It is one of the most versatile tools used for the observation of surface morphologies. For this study a JEOL JSM-IT300 InTouchScope™ Scanning Electron Microscope was used. The instrument produces an electron beam by thermionic emission from a tungsten filament, which can resolve features on the order of nanometres<sup>150</sup>. The electron beam interacts with atoms in the atomic layers near the surface, depending on the beam energy, causing secondary electrons as well as back-scattered electrons to be emitted, producing detectable signals that contain information about the sample's topography and composition. The electron beam is usually raster scanned across the prepared surface, producing a two-dimensional image. This instrument allows specimens to be observed under high or low vacuum, and offers a scan mode that inhibits charging artefacts, allowing non-conductive samples such as diamond to be characterised without prior surface metallisation. This equipment was used to study the surface structure of diamond samples and to observe crystal geometries, as well as to determine film thicknesses by viewing at 90 degrees to film growth.

### 3.2.2 Raman Spectroscopy

Raman Spectroscopy is a very useful technique for identifying molecular structure present in a sample by observing vibrational, rotational, and other low-frequency modes in a system<sup>151</sup>. It relies on monochromatic light, of frequency from the near infrared to the near ultra-violet, interacting with molecular vibrations and phonons in the sample, emitting light of a well-defined change in wavelength, corresponding to the vibrational energies of the bonds in the system. A spectrometer collects the emitted light and the technique provides a series of emission lines for analysis. There are multiple modes of scattering; Rayleigh refers to elastic scattering, which gives a strong line at the wavelength of the monochromatic light used to irradiate the system – this is typically filtered out. Raman, or inelastic, scattering gives weaker emission lines which appear symmetrically on either side of the Rayleigh line<sup>152</sup>. In solid samples at room temperature, the dominant Stokes lines (which appear on the low frequency side of the Rayleigh line) are used to give information about the lattice.

It is fast and non-destructive technique<sup>153</sup>, and furthermore, the intensity of a Raman emission line is directly proportional to the quantity of a certain species in the sample, making it invaluable to quantitatively estimate the relative amounts of different compounds in a system by comparison of the peak heights.

Pure diamond gives a sharp characteristic line at  $1332\text{ cm}^{-1}$ , with a full-width at half-maximum (FWHM) of ca.  $2\text{ cm}^{-1}$ <sup>154</sup>. Intentionally un-doped CVD synthetic diamond usually incorporates a small percentage of impurities, as well as other carbon species, such as graphite and amorphous carbon. Single-crystal graphite gives a single line at  $1575\text{ cm}^{-1}$ , whilst disordered graphite species give a line at  $1355\text{ cm}^{-1}$ . The relative intensities of these two emission lines are proportional to their quantities and inversely proportional to the graphite crystal size<sup>155</sup>. This enables the analysis of the quality of the CVD diamond, in terms of the ratio of the  $sp^2$  to  $sp^3$  species present, note however that this also depends on the excitation wavelength used.

A Renishaw 2000 instrument was used, in air and at room temperature, to acquire Raman spectra for the diamond films fabricated in this study. A laser excitation wavelength of  $514\text{ nm}$  (green,  $\text{Ar}^+$ ) was used.

### 3.2.3 Laser Micro-Machining System

A commercial laser micromachining setup (Oxford lasers Alpha 532-XYZ-A-U System) was used to cut substrates for diamond deposition, as well as to produce masks for HFCVD fabrication steps and etching of the substrates after deposition to aid in the wet etching process (see Section 3.1.2.4). The machine contains a  $532\text{ nm}$  wavelength diode-pumped solid-state nanosecond laser, which is capable of machining most common materials, including diamond. The setup enables micrometer-scale positioning and automatic control of the laser, with programmable settings for different processes.

**Table 3-1: System specifications of the laser micromachining system, according to the Oxford Lasers manual.**

Output	2.5 W at 5 kHz
Pulse Length	15 ns (FWHM) nominal
Pulse Frequency	10-50000 Hz
Max Speed (X, Y)	$200\text{ mm s}^{-1}$
Focal Length	100 mm (at $20\text{ }\mu\text{m}$ spot size)

During cut and etch processing, rapid heating by short-pulse focused laser causes local deformation of the material. Etch rate depends on the material and laser parameters used. This equipment was used primarily to cut and etch silicon substrates ( $500\text{ mm}$  thick), however it was also used to cut through diamond film (maximum thickness  $50\text{ }\mu\text{m}$ ). Diamond is transparent at wavelengths above  $227\text{ nm}$ , however, the surface graphitisation due to laser beam heating is sufficient to permit laser absorption<sup>156</sup>.

## 3.3 Electrical Characterisation

### 3.3.1 High resistance, I-V Curves

Samples were tested for resistance across the two attached wires using a lab multimeter (Fluke 287 True-RMS Electronics Logging Multimeter). If the major electrons transport route is through the i-diamond layer (not conduction around the surface), a high resistance in the order of  $\text{M}\Omega$  was expected. If the value is too low, it is indicative of an electrical short between the two boron-doped electrode layers.

To probe the current-voltage characteristics of the thin film diamond dynode structure, a high precision picoammeter (Keithley) was used. Measurements were done in air by applying high biasing voltage (DC PSU voltage source) to the seeded-side BDD layer

electrode, whilst the growth-side electrode was connected to ground. Low-noise triaxial cables connected the voltage source to the picoammeter. Voltages were applied in a ca. 10 V step-size, and current was logged by a LabView program built for the purpose. On applying the voltage step, the current signal was stable to within  $2 \times 10^{-7}$  A (standard deviation at -20 V with average value on the order of  $10^{-5}$  A). Current data values were logged every 0.5 seconds, for a length of 3 seconds at each voltage step, measured ca. 3 seconds after voltage step (enabled stabilisation if peak on step change). The final current measurement for each voltage was taken as an average over the measurement period and I-V curves were produced for each sample.

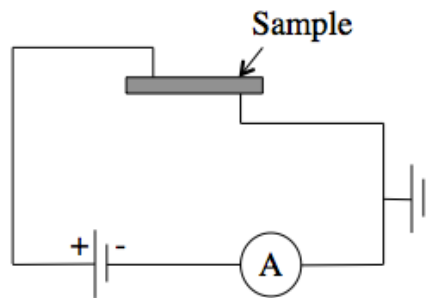


**Figure 3.9:** Circuit diagram of I-V measurement set up. Circuit involved a voltage source, an ammeter (connected to automatic logging program), and sample.

These I-V measurements are intended to analyse resistance through the samples, as well as ensuring ohmic contacts are fabricated, and not fabrication of Schottky barriers that arise as a consequence of mismatch between semiconductor and metal Fermi levels (Section 2.2.4).

### 3.3.2 Radiation Detector Behaviour

Once samples of desired electrical structure have been determined using the prior resistance/I-V curve analyses, samples were tested for radiation detector behaviour using a Ni-63 beta-emitting source, as in Figure 3.10. A 13.9 MBq Ni-63 foil  $\beta$ -particle source ( $7 \times 7 \times 0.1$  mm, maximum emission energy 67 keV, average emission energy 17 keV) will be held as close as possible to the seeded side (SS – the side that initially grew onto the Si, now exposed after removal of Si) of the sample whilst in the same electrical configuration as previously explained. The system will be held at applied bias, creating an electric field within the sample that should work to collect any electron/hole pairs excited by the incoming ionising particles. An increase in current on irradiation by beta particles would be suggestive of secondary electron emission.

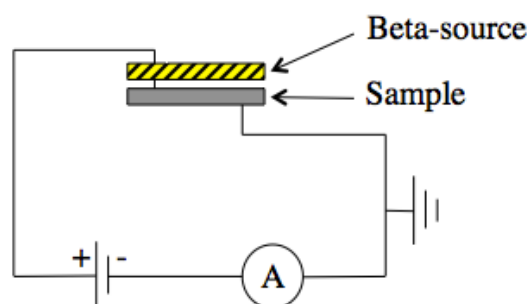


**Figure 3.10:** Circuit diagram of I-V measurement set up. Circuit involved a voltage source, an ammeter (connected to automatic logging program), a sample and a high-energy electron source Ni-63 resting on the sample. Note: beta-source was not connected to the circuit.

This  $\beta$ -particle irradiation was initially performed on simple i-diamond layer deposited on n-Si substrate, with no further processing other than to electrically connect the sample using silver conductive paint, shown in Figure 3.11 (a). There should be negligible electrical shorting around the surface or across the layers with this structure; as no BDD has been deposited, there would be little chance of electrical connection between the centre of the i-diamond layer and the centre of the n-Si substrate on the other side.

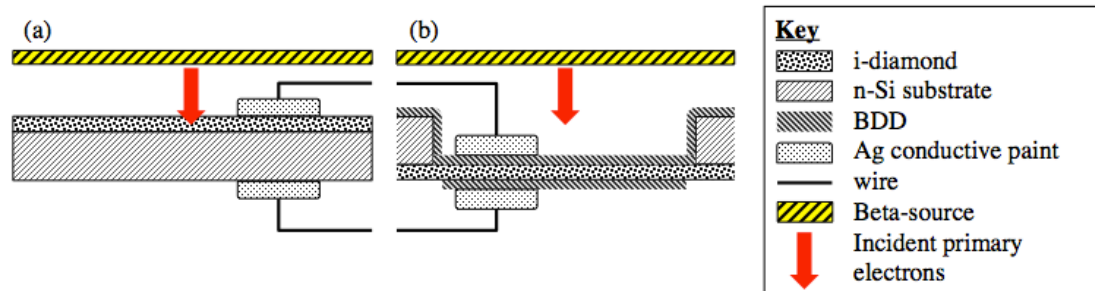


Figure 3.11: Schematic showing orientation of incidence of the Ni-63 source electron beam for; (a) interim structure of i-diamond layer supported by n-Si; (b) final diamond film dynode structure.

This  $\beta$ -particle irradiation test would have ideally been repeated on completed samples, however, the completed samples did not show the correct characteristics from prior testing to merit testing.

## 4 Results and Discussion

### 4.1 Structural Characterisation

Eleven samples were produced with varying i-diamond growth times. These were used to collect the data shown. Table 4-1 is given for reference.

**Table 4-1: Table of samples, growth time and measured properties. Blank values were not attained; film thicknesses could not be measured on account of only cracked samples being able to give a value; the crystal sizes could not be measured on account of the samples not being available at the same time as the SEM.**

<b>Sample-Number</b>	<b>Growth Time / hr</b>	<b>Film Thickness / <math>\mu\text{m}</math></b>	<b>Crystal Size / <math>\mu\text{m}</math></b>
S1	6	22.405	3.44
S2	2	7.304	1.24
S3	7	29.763	5.68
S4	5	22.54	4.04
S5	5		2.88
S6	4		
S7	4	22.14	
S8	6		4.62
S9	6		3.64
S10	7		5.78
S11	4.5		2.76

#### 4.1.1 Scanning Electron Microscopy (SEM) Characterisation

The crystal and overall film structure of the fabricated samples was evaluated using SEM, showing uniform thickness of the i-diamond layer across samples, as well as across growth times. Figure 4.1 shows SEM images of 4 different samples, imaged as freestanding films or whilst still on the Si substrate at 90 degrees to the film. Figure 4.1 (a)-(d) show the diamond crystal structure at the centre of the film after the sample had been cracked to reveal the side view. Refer to the figure caption for average thicknesses and growth times for each sample. Figure 4.1 (a) is the clearest to use to view the crystal growth structure due to it being the thinnest at 7.3  $\mu\text{m}$ . Crystals grow larger towards the surface, and the merging and disruptions of earlier crystals make way for the dominant ones. Figure 4.1 (e) shows a zoomed out image of (b), where the entire sample thickness is visible – i-diamond layer on Si substrate.

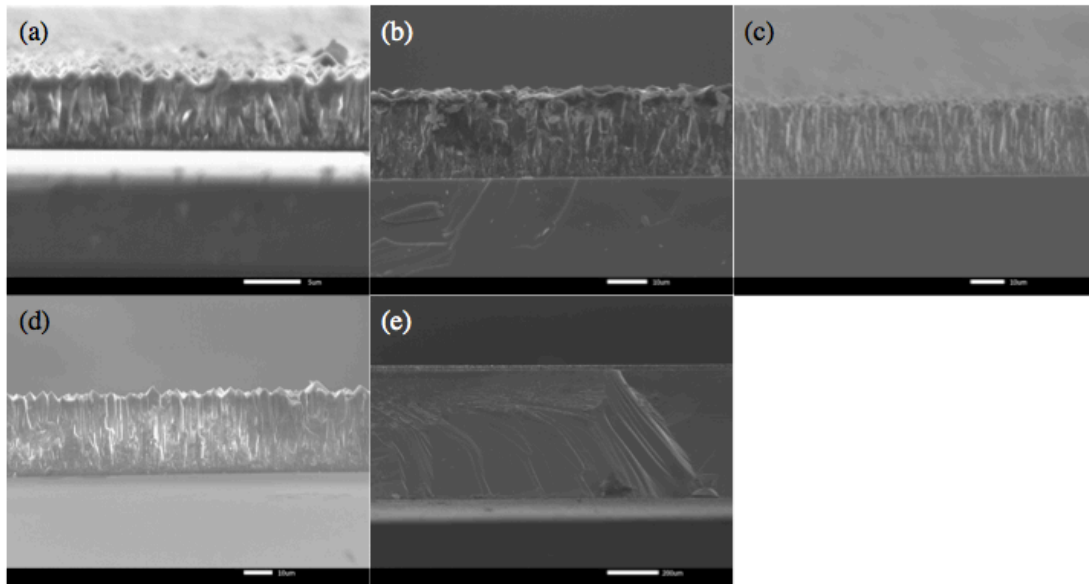


Figure 4.1: SEM images showing cutaways of i-diamond polycrystalline layer; (a) S2 - average thickness 7.3  $\mu\text{m}$ , 2 hours growth time, scale marker = 5  $\mu\text{m}$ , (b) S7 - average thickness 22.1  $\mu\text{m}$ , 4 hours growth time, scale marker = 10  $\mu\text{m}$ , (c) S4 - average thickness 22.5  $\mu\text{m}$ , 5 hours growth time, scale marker = 10  $\mu\text{m}$ , (d) S3 - average thickness 29.8  $\mu\text{m}$ , 7 hours growth time, scale marker = 10  $\mu\text{m}$ , (e) S7 - view of diamond layer on Si substrate, scale marker = 200  $\mu\text{m}$ .

Thicknesses were evaluated using the SEM software measuring ability, to evaluate a dependence on film thickness on growth time. Figure 4.2 shows this relationship, with a clear overall increase in thickness on increase in growth time, but with a plateau observed around the 4-6 hour mark. It is important to note that only one sample was evaluated for each data point, with error bars showing only standard deviation in thickness across a film, as opposed to across more substrates grown for the same length of time. The MW-CVD reactor was modified throughout the study, which could account for some variation in process variables and therefore affect the reliability across samples. A rough average growth rate of  $4 \mu\text{m h}^{-1}$  was found, ignoring initial dependence on nucleation points of film growth and initial reactor temperature instability.

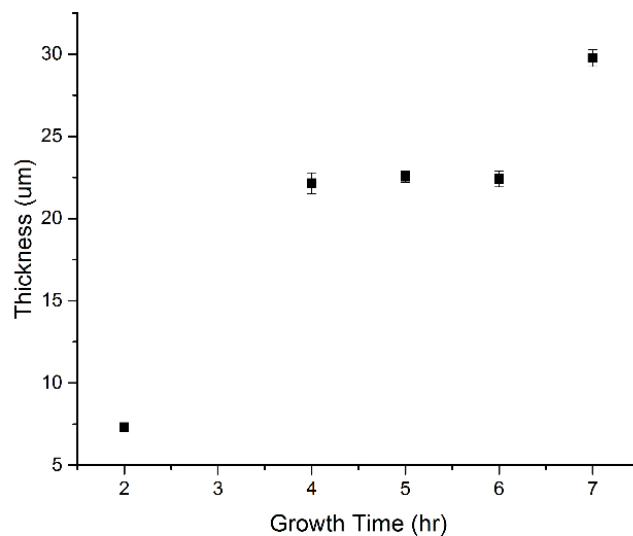
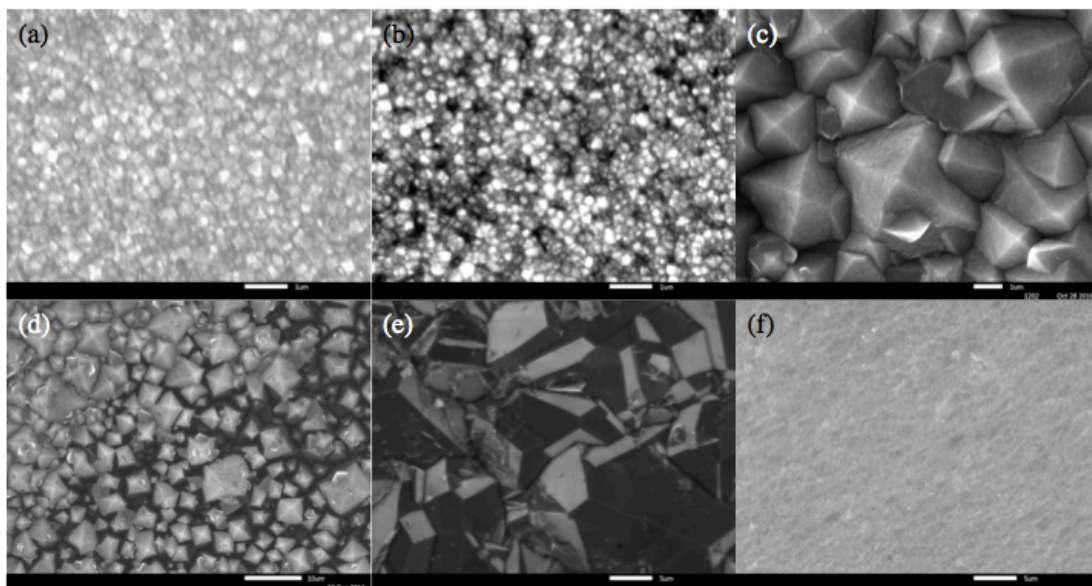


Figure 4.2: Film thickness plotted against i-diamond growth time. One sample measured for each growth length, so error bars shown relate to variation in thickness across one substrate grown for that length of time.

Surface morphologies of the samples were studied to observe surface quality and crystal sizes. Figure 4.3 shows 6 different sample surfaces varied across; (a) boron-doped diamond (BDD) grown on the seeded side of i-diamond layer; (b) shows the same on another sample (note the differences in image quality are down to the environment and variables used in the process of SEM imaging, and should not be compared); (c) growth surface of the i-diamond layer showing (111) crystal orientation, as expected for undoped diamond; (d) shows the same sample as (c) but zoomed out and at a different point on the surface, highlighting the tendency for some crystals to grow as tower-like structures without touching its neighbours (the darker areas surround crystal surfaces are deeper); (e) surface of a purely BDD film (acquired from Dr. S. Rosiwal<sup>1</sup>) for comparison with images (a) and (b); (f) shows the seeded side of the i-diamond film after Si removal.

The seeded surface of i-diamond (Figure 4.3 (f)) is very flat compared to the growth side, with poor quality crystal. It was very difficult to obtain a highly resolved SEM image of this surface, but simple microscopy showed a patterned structure on a different layer of resolution. Growing a layer of BDD on this surface should have increased the quality of the crystals at the interface. This has not been imaged.



**Figure 4.3:** SEM images of crystal sizes on the diamond growth surface; (a) S10, seeded side (SS) boron-doped diamond (BDD), scale marker = 1  $\mu\text{m}$ , (b) S8, SS-BDD, scale marker = 1  $\mu\text{m}$ , (c) S3, growth side (GS) i-diamond, scale marker = 1  $\mu\text{m}$ , (d) S3, GS-i-diamond, scale marker = 10  $\mu\text{m}$ , (e) 100  $\mu\text{m}$  thick HF-CVD BDD film (boron concentration  $1 \times 10^{19} \text{ cm}^{-3}$ ), acquired from Dr. S. Rosiwal, scale marker = 5  $\mu\text{m}$ , (f) S5, seeded side (SS) i-diamond, scale marker = 5  $\mu\text{m}$ .

The SEM software measuring ability was used to calculate average surface crystal size of the i-diamond layer growth. Figure 4.4 shows this dependence; with a linear fit (red line) giving a slope of  $0.697 \mu\text{m h}^{-1}$  and an intercept at  $-0.172 \mu\text{m}$ . It seems like the surface crystal size more than the film thickness tends to a linear dependence on the film growth time, but it is important to note that not all of the same samples were used for each data set.

<sup>1</sup> University of Erlangen-Nuremberg

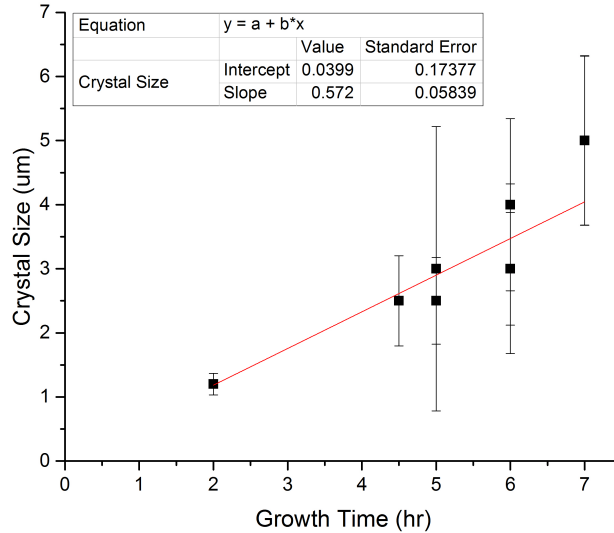


Figure 4.4: Growth surface crystal size (measured across crystal's diameter) plotted against i-diamond growth time. Error bars calculated from standard deviation of multiple crystals on each surface. The black squares are the average sizes of crystals for a particular sample, while the red line is a linear fit of the data points, with slope of  $0.697 \mu\text{m h}^{-1}$  and intercept at  $-0.172 \mu\text{m}$ .

Due to the nature of activation/deposition, the CVD carbon deposition was not limited to the horizontal surface, but also occurred over the sides of the substrate. For a short distance (up to  $100 \mu\text{m}$ ) over the edge, diamond (111) crystal growth dominated. Below this (for a few  $100 \mu\text{m}$ ), non-diamond carbon species dominated; while towards the bottom of the substrate, where it has contact with the hot substrate holder, the higher temperature causes graphitic deposits to be formed. Figure 4.5 demonstrates these growth deposits; (a) the larger side visible is the top of the substrate, with crystals shown growing over the edge; (b) and (c) show the substrates at 90 degrees, with the different regions of deposition clearly visible.

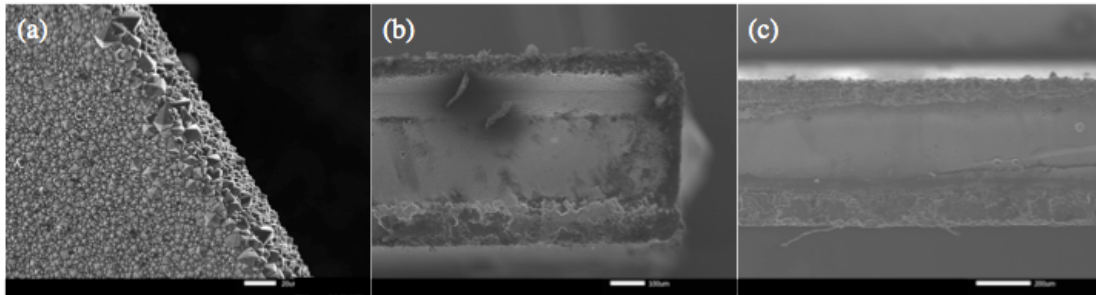


Figure 4.5: SEM images of samples showing growth over sides of substrates; (a) S4, major side visible is growth side i-diamond, scale marker =  $20 \mu\text{m}$ , (b) S9, edge and corner of substrate, where different carbon species are visible, scale marker =  $100 \mu\text{m}$ , (c) S7, edge of substrate, where different carbon species are visible, scale marker =  $200 \mu\text{m}$ .

A ca.  $2 \mu\text{m}$  thick layer of BDD grown on an i-diamond layer is hard to detect with certain spectroscopic methods, so SEM imaging was used to observe the difference of the surface before and after BDD deposition onto the seeded side of the i-diamond. This is shown in Figure 4.6, where (a) and (b) show one sample before deposition and after deposition images respectively, while (c) and (d) show similarly with another sample, with the two samples showing different magnifications. There is a clear uniform crystal structure on the 'after' images, which does not appear in the 'before' images. The growth surface of i-diamond has not been imaged with SEM after BDD deposition, and the surface's rough, large crystal, structure suggests that the success of uniform growth

cannot be extended to this second surface growth without analysis. It is possible that the BDD layer did not grow uniformly on this second side.

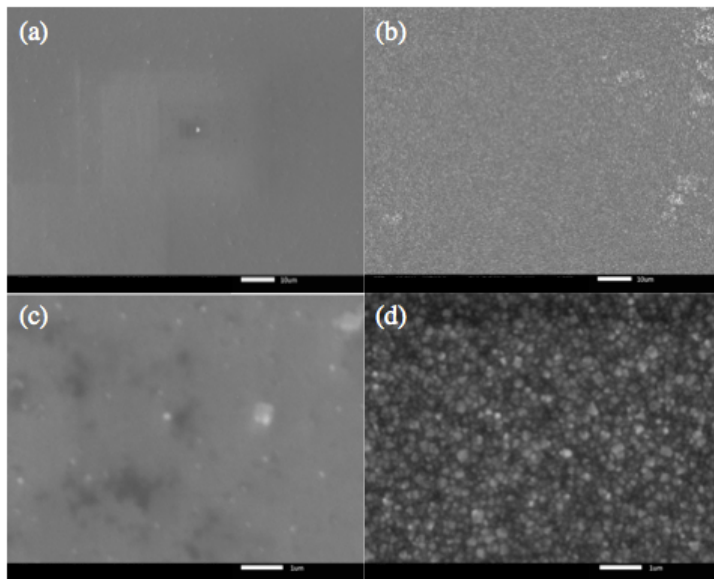


Figure 4.6: SEM images showing the seeded side (SS) of i-diamond layer before and after boron-doped diamond (BDD) growth; (a) S10, before BDD growth, scale marker = 10  $\mu\text{m}$ , (b) S10, after BDD growth, scale marker = 10  $\mu\text{m}$ , (c) S4, before BDD growth, scale marker = 1  $\mu\text{m}$ , (d) S4, after BDD growth, scale marker = 1  $\mu\text{m}$ .

A Si mask was used during the HF-CVD deposition of BDD on the growth surface of the i-diamond layer. The masking aimed to reduce BDD deposition around the edges of the sample, with an unmasked square portion in the middle where deposition could freely take place. It was assumed that due to the more linear propagation of gases towards the substrate of the HF-activation used in the reactor, that this may be an effective method of selective growth. SEM images (Figure 4.7) determine that although there is a decrease in BDD deposition under the mask, that it was not completely effective. Figure 4.7 (a) and (b) show the growth surface of the i-diamond layer unmasked and masked respectively. On the unmasked surface (a), there seem to be many smaller crystals interspersing the larger i-diamond crystals. These correlate with microscopic observations that seemed to show small crystals at a slightly higher resolution layer. On close inspection by polarised-light microscopy, there are crystal surfaces on the unmasked areas that display different refraction properties at different layers of resolution. These small crystals come across as small spots above the interfaces of the large crystals of the i-diamond surface. This could be indicative of a non-continuous layer of BDD.

SEM imaging requires careful preparation due to the charging effect of some surfaces by the electron beam. If a sample surface is not conductive, this is observed in brighter, less resolved images due to the collected charge. Figure 4.7 (c) shows a larger portion of the sample, with a dashed red line, above and to the right of which was where the sample was masked. As BDD is conductive, you would expect this area to be darker, with less charging. However, the i-diamond layer could have H-related adsorbates giving a surface conductivity, due to exposure to air over the period of a few weeks. It is not clear why the centre is brighter than the masked areas; however, the importance is that there is a difference between the two areas, showing that the mask was somewhat successful.

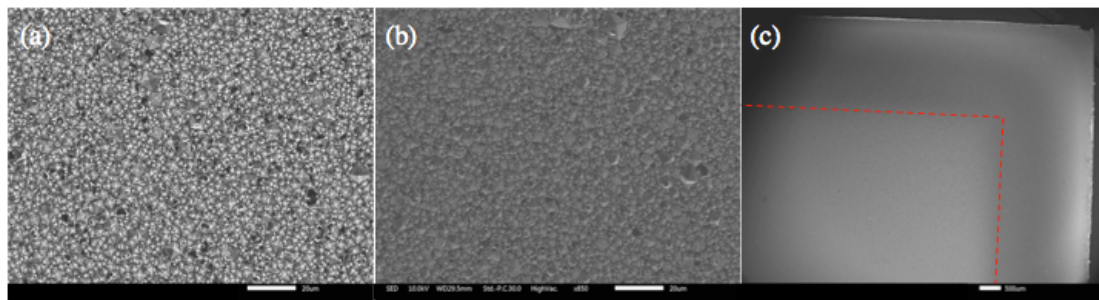


Figure 4.7: SEM images showing success of masking by Si-mask during HF-CVD boron-doped diamond (BDD) growth; (a) S8, growth side with BDD, scale marker = 20  $\mu\text{m}$ , (b) S8, growth side without BDD due to masking, scale marker = 20  $\mu\text{m}$ , (c) a zoomed-out view of S8, dashed red line showing where substrate was covered by mask during growth - darker patches at edge was covered, while inner square (paler) was not masked, scale marker = 500  $\mu\text{m}$ .

#### 4.1.2 Raman Spectroscopy Analysis

Raman spectra of the fabricated samples at various steps of the process indicate reliable CVD deposition of the i-diamond films. This is shown by the very similar values across the acquired spectra; of the peaks and full-width half-maximum measurements. A rising baseline was observed in all of the spectra of the samples. This is expected to be due to a large photoluminescent (PL) background, upon which the rest of the smaller Raman features sit<sup>157</sup>. This background decreased, as expected, with the boron-doped samples, as the B may be compensating the nitrogen-related defects within the diamond that cause the majority of the photoluminescence. However, none of the samples were completely free of it, and all had it to some varying extent. Therefore, in order to be able to analyse and compare the samples, this PL background was subtracted. A fourth order polynomial curve was fit to the background and subtracted from the original spectrum. This process is illustrated in Figure 4.8.

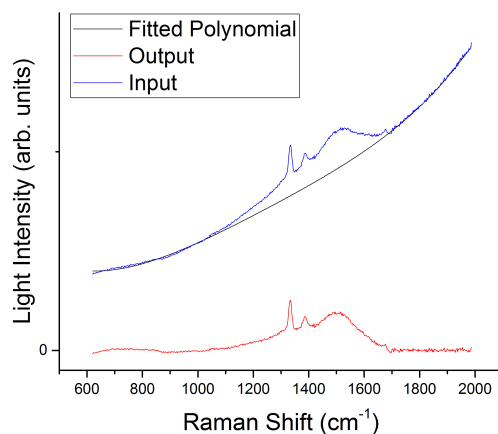
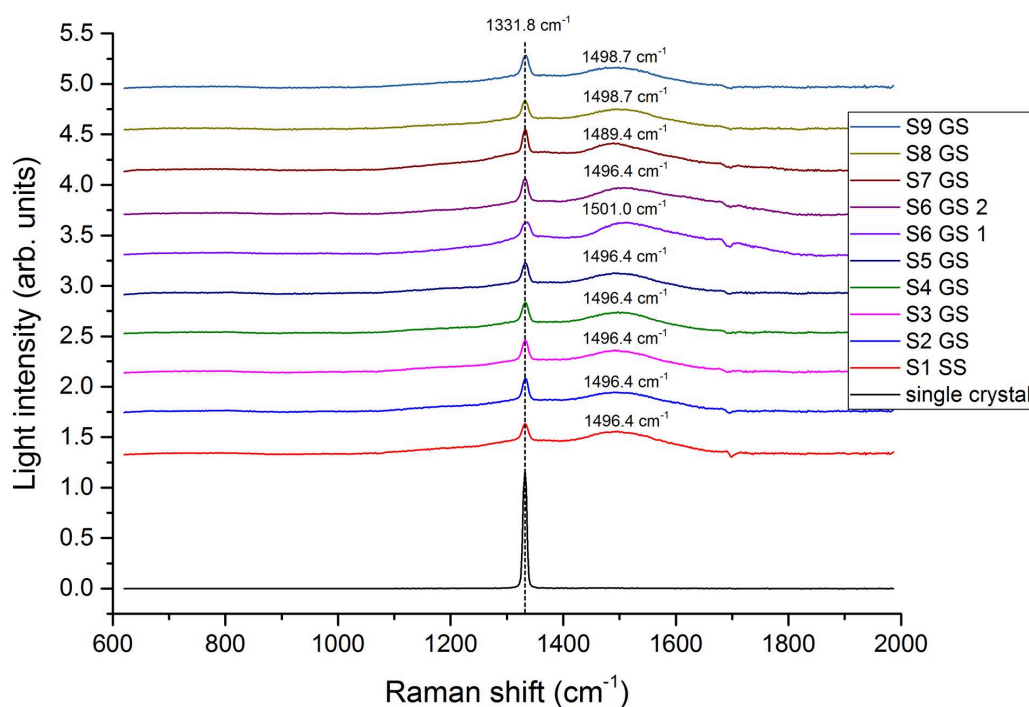


Figure 4.8: Example of a PL background subtraction from the Raman spectrum of an i-diamond sample taken using a green (514 nm) excitation. The black line is the fitted PL background polynomial, the blue line was the input Raman spectrum, whilst the red line shows the new spectrum with baseline removed.

The Raman spectra of the samples - i-diamond and BDD on i-diamond - excited in the green (514 nm) are shown in Figure 4.9 and Figure 4.10. Figure 4.9 shows the spectra for the samples taken just after initial i-diamond layer deposition on Si substrate. The observed peak at 1331.8  $\text{cm}^{-1}$  was assigned to pure diamond's characteristic peak (1332  $\text{cm}^{-1}$ ), however, calculated values of full-width at half-maximum, at an average of ca. 12  $\text{cm}^{-1}$ , are higher than those of pure diamond (ca. 2  $\text{cm}^{-1}$ ) (Section 3.2.2). The large grain boundaries as well as  $\text{sp}^2$  carbon species within these boundaries are the cause of this

widening, as well as defects and nitrogen-impurities within the films. The other main peak of the i-diamond spectra of ca. 1497  $\text{cm}^{-1}$ , which does not correspond to the graphite peak, and no evidence of what this may be can be found in the literature surrounding CVD diamond. However, Raman peak assignment<sup>158</sup> suggests that this peak could be due to aromatic ring chain vibrations,  $\text{CH}_2$  or  $\text{CH}_3$  (asymmetrical) species. As explained in Section 2.4.2.1, any of these species can terminate the dangling reactive surface sites during deposition. It is expected that the graphite peak is present and a part of these non- $\text{sp}^3$  carbon species.



**Figure 4.9:** Raman spectra of samples following i-diamond layer deposition using green (514 nm) excitation. S's refer to sample numbers as used throughout the Results and Discussion Section, see Table 4-1. GS refers to growth side. The spectra have been offset vertically from each other for clarity, with PL background removed to produce a flat baseline. A single crystal diamond sample was used for comparison, and each of the further spectra shared the common diamond peak at 1331.8  $\text{cm}^{-1}$ , with another peak ca. 1497  $\text{cm}^{-1}$ . Two spectra were acquired for S6 because it did not grow an even i-diamond layer, so a spectrum was acquired for the uneven (S6 GS 1) and even (S6 GS 2) sections of the film.

One of the samples (S6) has two Raman spectra associated because i-diamond layer growth was poor, leaving a barely coated substrate at the centre and film growth only at the sides. The first spectrum (S6 GS 1) was taken at the centre where the film growth was poor, while the second (S6 GS 2) was taken at the edge. S6 GS 1 shows a different spectrum to the others, with a longer non- $\text{sp}^3$  carbon species peak tail to the right, and a much larger FWHM for the pure diamond peak (1331.8  $\text{cm}^{-1}$ ).

Figure 4.10 shows the spectra for the samples taken after BDD deposition on the seeded side of the i-diamond layer (four spectra were taken at different positions on S8 and S4). The observed peak at 1331.8  $\text{cm}^{-1}$  continued throughout these spectra, with barely any shift even with the BDD layer present. This is mostly because it is difficult to focus the Raman laser on such a thin layer and was likely acquiring data from deeper within the sample – into the i-diamond layer. The peak observed ca. 1497  $\text{cm}^{-1}$  has been shifted slightly from the non-BDD samples, with negligible difference between the BDD samples. This shift could be due to the insertion of boron into the carbon lattices,

weakening the bonds on average, as a B-C bond is weaker than a C-C bond<sup>159</sup>. This is indicative of the presence of boron atoms in the carbon lattice.

There is one other detectable peak at 1386.2 cm<sup>-1</sup> for the spectrum of S8 BDD. This is likely indicative of a CH<sub>3</sub> species present on the surface or at the grain boundaries.

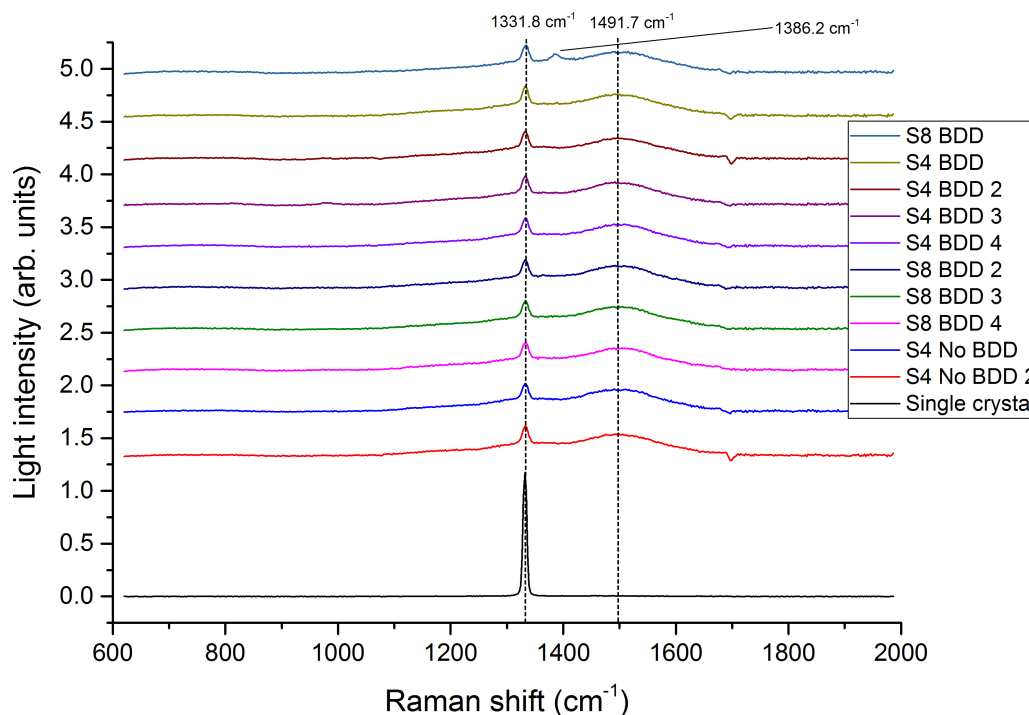


**Figure 4.10: Raman spectra of samples following boron-doped diamond layer deposition on the exposed seeded side of the i-diamond layer after removal of the Si substrate, using green (514 nm) excitation. S's refer to sample numbers as used throughout the Results and Discussion Section, see Table 4-1. The spectra have been offset vertically from each other for clarity, with PL background removed to produce a flat baseline. A single crystal diamond sample was used for comparison, and each of the further spectra shared the common diamond peak at 1331.8 cm<sup>-1</sup>, with another peak ca. 1497 cm<sup>-1</sup>. The spectra of S8 BDD showed another peak at 1386.2 cm<sup>-1</sup>. The spectra labelled 'No BDD' relate to measurement of the seeded side (SS) of the i-diamond layer, prior to BDD deposition. These show no obvious difference to the others.**

To obtain values of FWHM, the diamond band centred at 1331.8 cm<sup>-1</sup> was fitted to a Gaussian curve. These values are indicative of the quality of the diamond film, with an increase in FWHM showing lesser quality. The single diamond crystal was tested first for control purposes. The high value of ca. 7.6 cm<sup>-1</sup> is much higher than the reported 2 cm<sup>-1</sup>, perhaps due to poor calibration of the Raman setup. Therefore, when observing the relatively high values of ca. 12-13 cm<sup>-1</sup> found for the samples, it is important to consider that the effective values may be lower. Bar the value of 17.7 cm<sup>-1</sup> for the defective S6 (poor i-diamond layer growth), all of the samples bear a similar FWHM value, showing reliability across samples of diamond quality.

Table 4-2: FWHM values for the 1331.8 cm<sup>-1</sup> diamond Raman peak.

Sample-Number	Growth Time / hr	FWHM / cm <sup>-1</sup>			
		Test Sample	BDD on SS	SS of i-diamond	GS of i-diamond
Single crystal diamond	N/A	7.617			
S1	6			13.103	
S2	2				11.944
S3	7				12.328
S4	5		12.831	12.683	13.665
S5	5				13.050
S6	4				17.712
S7	4				10.566
S8	6		13.430		13.306
S9	6				13.971

## 4.2 I-V Characteristics

Initial resistance measurements found that most samples showed very little resistance across the sample, in the order of a few kΩ. This is far too low for the heavily insulating i-diamond layer, so there must be some form of surface conduction of electrons taking place. When the I-V characteristics of these samples were tested, linear ohmic curves were found, indicative of successful ohmic contacts at the junctions.

The interim structures discussed in Section 3.3.2, named S7.Delam and S7.Scratch due to identifiable surface features were probed for I-V characteristics, shown in Figure 4.11 and Figure 4.12 respectively. These both show ohmic behaviour, indicative of an ohmic junction at the i-diamond to n-Si layers (Section 2.2.4). The trends are not perfectly linear, with slight kinks at applied voltage = - 50 V for S7.Delam, and ± 40 V for S7.Scratch. These are due to the picoammeter having different ammeters for different current ranges.

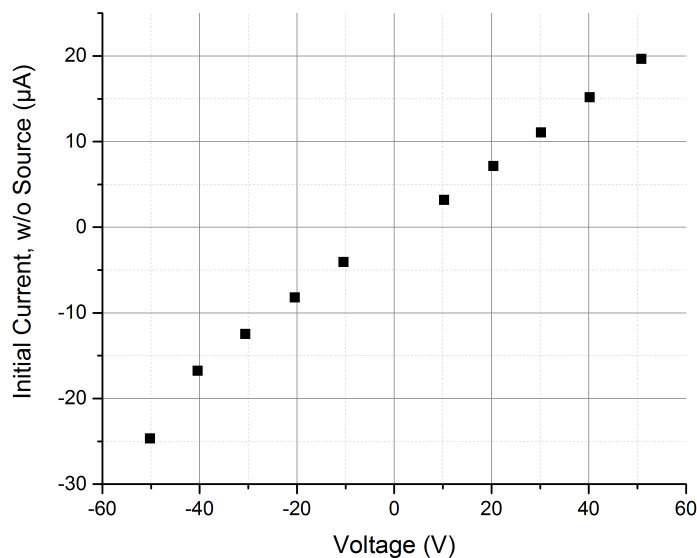
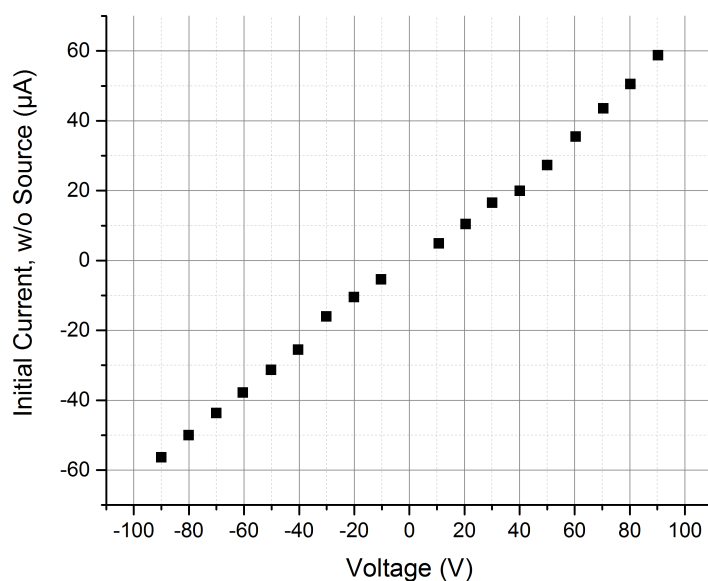


Figure 4.11: I-V data for S7.Delam (S7 split into two halves, “Delam” due to an identifiable delamination on the diamond surface). Clear ohmic behaviour is visible. Fitted slope of  $0.411 \times 10^{-6} \Omega^{-1}$ .



**Figure 4.12: I-V data for S7.Scratch (S7 split into two halves, “scratch” due to an identifiable scratch on the diamond surface). Clear ohmic behaviour is visible. Fitted slope of  $0.615 \times 10^{-6} \Omega^{-1}$ .**

Fitting slopes to the curves (not shown) gave values of  $0.411 \times 10^{-6} \Omega^{-1}$ , and  $0.615 \times 10^{-6} \Omega^{-1}$  for ‘Delam’ and ‘Scratch’ respectively, giving resistances of  $2.43 \pm 0.07 \text{ M}\Omega$  and  $1.63 \pm 0.02 \text{ M}\Omega$  respectively. These values in the  $\text{M}\Omega$  order are indicative of successful transport of electrons through the substrate layers as opposed to around them.

I-V curves were fitted for the lower resistance final structure samples too, one of which is shown in Figure 4.13. The fitted slope gave a value of  $9.91 \times 10^{-6} \Omega^{-1}$ , giving a resistance of  $100.9 \pm 0.2 \text{ k}\Omega$  (only shown to 4 s.f. to enable error inclusion). This is a much higher resistance, indicative of some sort of surface conduction. Prior to this measurement, the edges of the samples were laser etched to remove any side-growth conduction mechanisms, and cleaned in boiling acid to remove any graphitic species. This treatment was expected to remove any graphitic conduction mechanisms, as well as remove any H-species adsorbates that could be aiding the surface conductivity. It is unclear as to what is causing such a low resistance in the structure.

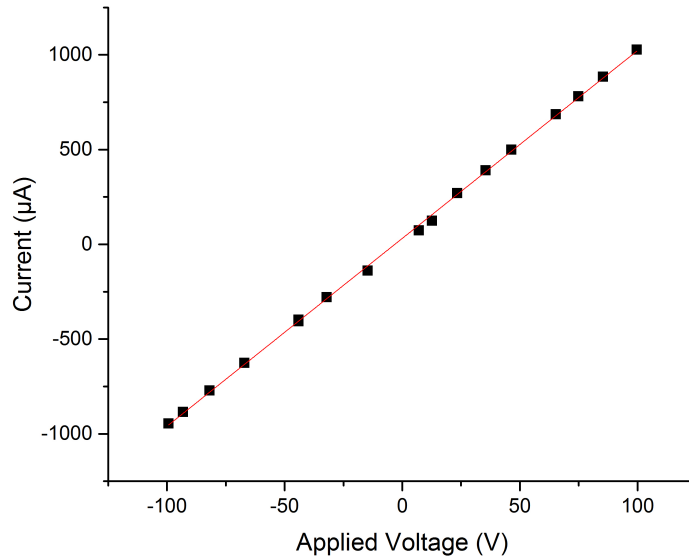


Figure 4.13: I-V data for S11. Clear ohmic behaviour is visible. Fitted slope of  $0.9.91 \times 10^{-6} \Omega^{-1}$ .

#### 4.2.1 Diode Behaviour

Throughout the project, the fragility of the samples caused them to crack through certain processes and mishandling. S8 cracked, prior to acid cleaning, and on I-V curve measurement showed diode behaviour as shown in Figure 4.13. This is indicative of a Schottky barrier between the junctions in the sample. It is unclear why none of the other samples showed the same behaviour, as they all received the same processing and hence should be of the same structure.

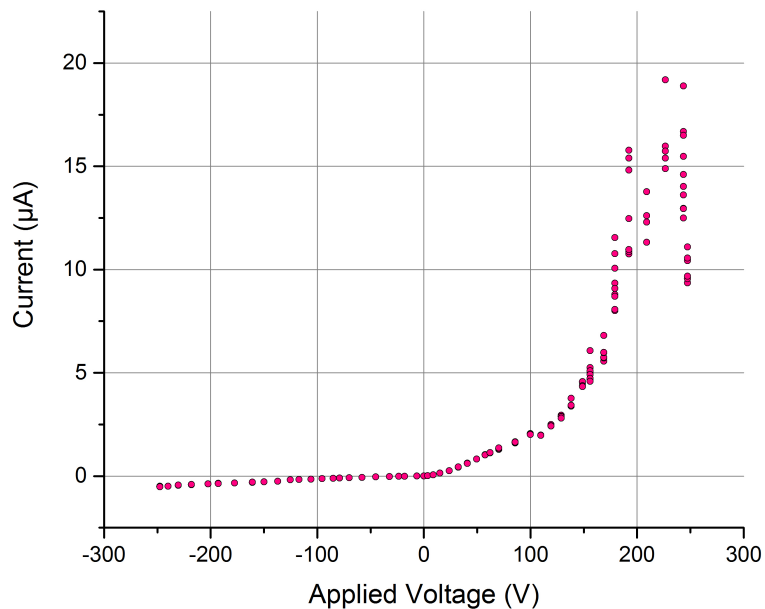


Figure 4.14: I-V data for S8.1 (a cracked piece of S8). Diode behaviour observed.

A paper focused on p-i-p structures and their response to radiation<sup>160</sup> suggests reasons as to this diode behaviour. The N-impurities in the bulk of the i-diamond could drastically affect the properties of the initial p-i junction, producing a potential barrier at the junction interface. This p-i junction on diamond is formed by electrical activation of the deep donors/donor-like traps by the holes diffused out of the p-type region<sup>161</sup>. This potential barrier formed in many similar structures causes the principle movement

of electrons into the device to be by thermionic emission (TE). The originally neutral traps of the i-layer are ionised in the positive space charge layer of the i-layer gap, shifting their energy levels above the Fermi level. Therefore, electron transport through the p-i-p diode is governed by the TE of holes across the forward biased p-i junction (as long as this voltage exceeds the voltage required for the reach-through condition).

### 4.3 i-Diamond/n-Si Radiation Detector Behaviour

There is a clear trend on irradiation by beta-particles that a *decrease* in absolute current occurs when the sample was in the presence of the Ni-63 beta-particle source. This is shown in Figure 4.15. Curves of current against time for each voltage (S7.Scratch – interim structure) are plotted on the same graph, to show I-V relationship for each measurement, as well as showing the change in current on irradiation (introduction of source = 15 s, removal of source = 45 s). An *increase* in current was expected on irradiation, to signify an increase of carriers due to electron/hole pair generation caused by electron bombardment.

Although it is not clear whether secondary electron emission is occurring, there is an effect on the device’s performance on irradiation by Ni 63 beta-particle source to the system. This at least supports the structure for diamond radiation detector applications.

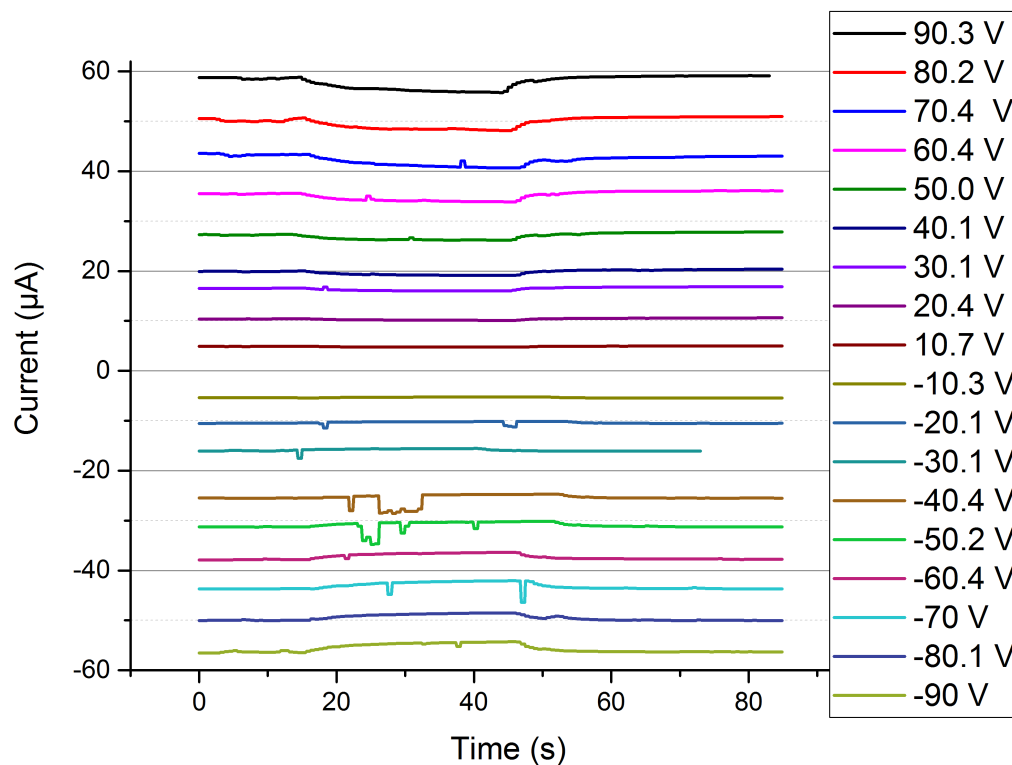


Figure 4.15: Combined graph of current against time with introduction of ionising beta-particle source Ni-63 at 15 seconds, and removal at 45 seconds (sample ID: S7.Scratch).

Figure 4.15 shows odd peaks that are down to accidental movement of the source during data collection. These can be neglected when considering the curves for further analysis. Therefore, in Figure 4.16, these have been removed and replaced with extrapolated curves to allow for clearer observation. Each of the curves from Figure 4.15 were modified by multiplying the ones with negative bias by  $-1$  to give absolute comparable values, as well as removing the base current at each bias voltage. Proportionally, the curves obtained at lower voltages showed a smaller decrease in current, while the positive voltage (of a positive and negative voltage pair) showed a

larger decrease than its negative counterpart. The i-n (i-diamond/n-type Si) structure somewhat explains this, due to the beta-source being an input of excess of electrons. The high electron input flux is always focused on the i-diamond surface, while the bias is flipped between forward and reverse. This behaviour identifies slight diode behaviour, which would be possible with an i-n structure. It is also important to consider the N-impurities present in the i-diamond, which give it a slight level of n-doping, creating a p-n junction.

The gradual decrease in current on irradiation getting to a final plateau, as opposed to a current step as observed with changing the voltage, displays charging of the material. There is also a gradual increase in current back to initial current once the source has been removed – a discharging effect. This charging behaviour and the decrease in current on irradiation suggests that the nitrogen impurities present in the bulk of the i-diamond layer act as traps for carriers. As electrons enter and possibly generate electron/hole pairs, the traps collect these carriers, heavily reducing carrier paths, thus reducing possible SEY. The curve starts to plateau as the traps fill up.

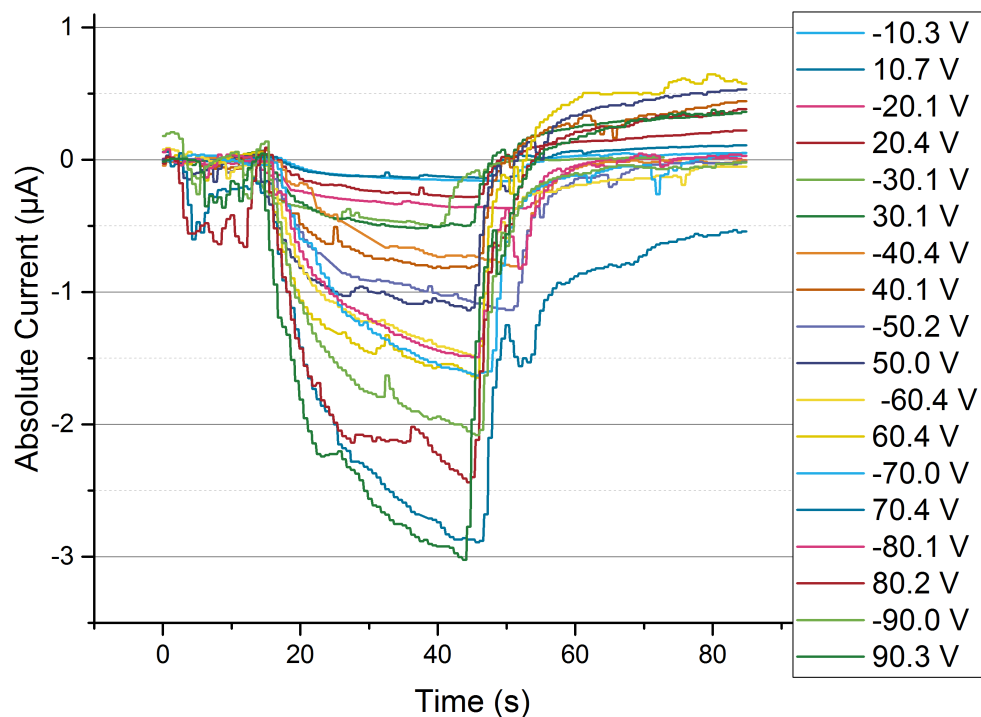


Figure 4.16: Current versus time graphs from Figure 4.15 were all modified to show the same orientation (the values for negative bias were multiplied by - 1) and had their base currents removed so that they could be superimposed for comparison.

A calculation of the possible temperature increase in the i-diamond film per second of irradiation; when taking volume to be  $1.1 \times 10^{-9} \text{ m}^3$  ( $22 \mu\text{m} \times 5 \text{ mm} \times 10 \text{ mm}$ ), incoming number of electrons a second to be  $13.9 \times 10^6$  (maximum possible activity of the Ni-63 source), specific heat capacity to be  $6.61 \text{ J mol}^{-1} \text{ K}^{-1}$ , and molar mass of carbon to be  $12.03 \text{ g mol}^{-1}$ ; gives a value of  $1.04 \times 10^{-6} \text{ }^\circ\text{K}$ . This is negligible and therefore cannot take into account any increase in resistance due to temperature increase.

Calculation of possible increase in current due to secondary electron emission yields the small value of  $2.36 \times 10^{-9} \text{ A}$  in one second; calculated using the maximum possible activity of the source, and the suggested average SEY for each primary electron at its average energy of 17.43 keV. Even this is a positive estimate as there are many loss mechanisms that have not been considered in the calculations. This relates to  $0.000236 \mu\text{m}$  by the scale of the graphs shown. This is a negligible value on the scale of the

changes in current observed, suggesting that SEE could indeed be occurring, but that our system was not set up to be able to observe it.

#### 4.4 Conclusion

The possibilities of diamond's large secondary electron yield, as well as its other outstanding physical and chemical properties, present diamond as a very successful material for electron multiplication. The concept envisioned in this study has several advantages over conventional structures for electron multiplication. The BDD/i-diamond/BDD p-i-p structure gives homojunctions for increased crystal quality on either side of the i-diamond film. BDD is itself used for secondary electron emission, which proves it a very interesting contact material. Unfortunately, SEE could not be confirmed from the radiation-detector proof-of-concept test. The proof of concept radiation tests showed a *decrease* in current on irradiation by Ni-63 beta-particles. An amplified signal - caused by extra carriers generated by the high-energy electron beam - would ideally be detected, with an increase in the current collected by the second electrode. The results did, however, correlate with previously found data regarding the p-i-p I-V diode behaviour. Further investigation is required to further this work. The process of fabrication of the structure was discussed and multiple structural and electrical characterisation techniques were shown. A growth rate of  $4 \mu\text{m h}^{-1}$  was achieved for deposition of undoped diamond, with uniform thicknesses and crystal sizes achieved. Raman spectroscopy showed peaks at  $1331.8 \text{ cm}^{-1}$  with FWHM values of ca.  $12 \text{ cm}^{-1}$ , which is on the order of values found in recent literature. A uniform boron-doped diamond layer was successfully deposited on the i-diamond exposed seeded-surface, with evidence shown by SEM imaging and Raman analysis. Some success of boron-doped diamond deposition on the growth surface of i-diamond was established, but further analysis would be required to confirm this. I-V characteristics of interim and final diamond film dynode structures were investigated, showing mostly ohmic behaviours.

There were difficulties throughout the project, regarding fragility of the samples and ability to grow uniform BDD layers on the growth surface of the i-diamond layer. Selective growth of BDD in the HF-CVD reactor showed promise, however it did not solve the issue of surface conduction. Due to surface conduction, the final structure samples did not merit testing for radiation detector behaviour; however, the interim structure samples worked successfully as radiation detectors. Methods of each fabrication process were optimised and a successful method of handling the films was established.

## 5 Future Work

Taking the project forward, there are a number of tasks that could be advantageous. These include looking further into the work surrounding the BDD layer deposition on the growth surface; process optimisation is required. Hall resistance measurements should be undertaken with caution – this characterisation method was extremely successful at cracking samples.

Other possible structures should be considered, by changing the electrode materials, or even having an asymmetrical structure; a transparent metal layer on the input side to reduce absorption of electrons on impact, with the BDD layer on the output face.

It would be ideal to identify the point at which surface conduction – or essentially the cause of the low resistance across the sample – enters the fabrication process. A step-by-step analysis should be undertaken to resolve this problem.

Emitted energy distribution curves would be a good evaluation for success of samples and their surface properties, whether this be an NEA allowing ejection of the thermalized electrons within the conduction band, or the initial surface allowing electrons into the sample. The radiation detector experiment should be repeated, with more controls to give more convincing results. An E- $\Delta$ E set up could be used, to probe charge collection efficiency and to give accurate secondary electron yield results. Leakage current, and other properties of the device should be analysed to compare the material with solid-state devices for the future lifetime of the research.

The amounts of impurities within the samples (e. g. nitrogen) could be quantified from integrated fluorescence intensity, to create a more solid background to the work where irradiation by electron beam shows N-traps as being a major part of the principle.

## 6 References

---

- <sup>1</sup> H. Bruining, *Physics and Applications of Secondary Electron Emission*, McGraw-Hill Book Co., New York, 1954.
- <sup>2</sup> Hackenberg, W. Brauer, in *Secondary Electron Emission from Solids Vol. XI*, Academic Press, New York, 1959, Advances in Electronics and Electron Physics.
- <sup>3</sup> A. J. Dekker, in *Secondary Electron Emission Vol. 6*, Academic Press, New York, 1958, Solid State Physics.
- <sup>4</sup> R. O. Jenkins, W. G. Trodden, *Electron and Ion Emission*, Dover, New York, 1965, p.54.
- <sup>5</sup> A. Shih *et al.*, *Applied Surface Science*, 1977, **111**, 251-258.
- <sup>6</sup> C.A. Klein, *J. Appl. Phys.*, 1968, **39**, 2029.
- <sup>7</sup> K.L. Jensen *et al.*, *J. Appl. Phys.*, 2010, **108**, 044509.
- <sup>8</sup> V.V. Dvorkin *et al.*, *Diamond and Rel. Mat.*, 2003, **12**, 2208-2218.
- <sup>9</sup> Please refer to reference-5
- <sup>10</sup> Please refer to reference -9
- <sup>11</sup> V.H. Ritz *et al.*, *Surf. Interface Anal.*, 1992, **18**, 514.
- <sup>12</sup> A.J. Dekker, in *Solid State Physics*, ed. F. Seitz and D. Turnbull, Academic Press, New York, 1958, Advances in Research and Applications, p.251.
- <sup>13</sup> Please refer to reference -13
- <sup>14</sup> E. Wang *et al.*, *Phys. Rev. ST Accel. Beams*, 2011, **14**, 061302.
- <sup>15</sup> G. F. Knoll, *Radiation Detection and Measurement*, John Wiley and Sons, 2000.
- <sup>16</sup> H. Raether, *Electron avalanches and breakdown in gases*, Butterworths, 1964.
- <sup>17</sup> S. M. Sze, *Physics of Semiconductor Devices*, John Wiley & Sons, 1981, p.45.
- <sup>18</sup> Townsend image, [https://en.wikipedia.org/wiki/Townsend\\_discharge](https://en.wikipedia.org/wiki/Townsend_discharge), (accessed 25/04/17).
- <sup>19</sup> C. Bouchard, J.D. Carette, *Surf. Sci.*, 1980, **100**, 251.
- <sup>20</sup> Please refer to reference -4
- <sup>21</sup> G.T. Mearini *et al.*, *Thin Solid Films*, 1994, **253**, 151.
- <sup>22</sup> G.T. Mearini *et al.*, *Surf. Int. Anal.*, 1994, **21**, 138.
- <sup>23</sup> D.P. Malta *et al.*, *Mat. Res. Soc. Syrup. Proc.*, 1994, **339**, 39.
- <sup>24</sup> D. Takeuchi *et al.*, *Diamond Relat. Mater.*, 2008, **17**, 986.

- 
- <sup>25</sup> D.P. Malta *et al.*, *Mat. Res. Soc. Syrup. Proc.*, 1996, **416**, 311.
- <sup>26</sup> H.J. Hopman *et al.*, *Diamond Relat. Mater.*, 1999, **8**, 1033-1038.
- <sup>27</sup> F.J. Himpsel *et al.*, *Phys. Rev. B*, 1979, **20**, 624.
- <sup>28</sup> Please refer to reference -5
- <sup>29</sup> Please refer to reference -5
- <sup>30</sup> Please refer to reference -5
- <sup>31</sup> R. Nemanich, *Diamond negative electron affinity surfaces, structures and devices*. No. CONF-950840--. Government Printing Office, Washington, DC (United States), 1995.
- <sup>32</sup> R. J. Nemanich *et al.*, *MRS Bulletin*, 2014, **39**, 490–494.
- <sup>33</sup> Please refer to reference -28
- <sup>34</sup> S.X. Tao *et al.*, *Materials*, 2016, **9**, 1017.
- <sup>35</sup> Please refer to reference -28
- <sup>36</sup> Please refer to reference -32
- <sup>37</sup> K.M. O'Donnell *et al.*, *Phys. Rev. B*, 2010, **82**, 115303.
- <sup>38</sup> K.M. O'Donnell *et al.*, *Phys. Rev. B*, 2015, **92**, 035303.
- <sup>39</sup> X.Y. Chang *et al.*, *Phys. Rev. Lett.*, 2010, **105**, 164801.
- <sup>40</sup> I. Lin *et al.*, *MRS Bulletin*, 2014, **39**, 533-541.
- <sup>41</sup> B.D. Thoms *et al.*, *J. Appl. Phys.*, 1994, **75**, 1804.
- <sup>42</sup> K.M. O'Donnell *et al.*, *Adv. Funct. Mater.*, 2013, **23**, 5608.
- <sup>43</sup> M.I. Landstrass, K.V. Ravi, *Appl. Phys. Lett.* 1989, **55**, 975.
- <sup>44</sup> F. Maier *et al.*, *Phys. Rev. Lett.*, 2002, **85**, 3472.
- <sup>45</sup> M.I. Landstrass *et al.*, *Appl. Phys. Lett.*, 1989, **55**, 975–977.
- <sup>46</sup> W. Zhang *et al.*, *Phys. Rev. E.*, 2008, **78**, 041603.
- <sup>47</sup> F.B. Liu *et al.*, *Acta Phys. Sin.*, 2008, **57**, 1171.
- <sup>48</sup> B. Rezek *et al.*, *Appl. Phys. Lett.*, 2003, **82**, 3336.
- <sup>49</sup> Article: "A 25-Year Battery: Long-lived nuclear batteries powered by hydrogen isotopes are in testing for military applications, Katherine Bourzac, Technology Review, MIT, 17 Nov 2009.", <https://www.technologyreview.com/s/416312/a-25-year-battery/>, (accessed 25/04/17).

- 
- <sup>50</sup> G. Audi *et al.*, *Nuclear Physics A*, 2003, **729**, 3-128.
- <sup>51</sup> H. Semat, J.R. Albright, in *Introduction to Atomic and Nuclear Physics*, Chapman and Hall, London, 5th ed., 1972, ch. 4.12.
- <sup>52</sup> P. Bergonzo *et al.*, *Physica Status Solidi A*, 2001, **185**, 167.
- <sup>53</sup> P.K. Baumann, R.J. Nemanich, in *Low-Pressure Synthetic Diamond: manufacturing and applications*, ed. B. Dischler and C. Wild, Springer-Verlag, Berlin Heidelberg, 2000, chapter 15, 281-303.
- <sup>54</sup> C.E. Nebel *et al.*, *J. Phys. D - Applied Physics*, 2007, **40**, 6443.
- <sup>55</sup> D.M. Trucchi *et al.*, *Diamond and Related Materials*, 2006, **15**, 827-832.
- <sup>56</sup> M.L. Perl, L.W. Jones, *Optical Feedback Image Intensifying System*, 1964, U.S. Patent 3,154,687.
- <sup>57</sup> M. Pomorski *et al.*, *Appl. Phys. Lett.*, 2013, **103**, 112106.
- <sup>58</sup> V. Grilj *et al.*, *Appl. Phys. Lett.*, 2013, **103**, 243106.
- <sup>59</sup> J. Isberg *et al.*, *Science*, 2002, **297**, 1670.
- <sup>60</sup> D. Dobos, H. Pernegger, *Nucl. Instrum. Methods Phys. Res. A*, 2011, **628**, 246.
- <sup>61</sup> M. Ciobanu *et al.*, *IEEE Trans. Nucl. Sci.*, 2011, **58**, 2073.
- <sup>62</sup> J. Pietraszko *et al.*, *Nucl. Instrum. Methods Phys. Res.*, 2010, **1**, 121.
- <sup>63</sup> K. Desjardins *et al.*, *J. Phys.: Conf. Ser.*, 2013, **425**, 212004.
- <sup>64</sup> J. Morse *et al.*, *MRS Proceedings*, 2007, **1039**.
- <sup>65</sup> J. W. Keister *et al.*, *Nucl. Instrum. Methods Phys. Res. A*, 2011, **649**, 91-93.
- <sup>66</sup> B.E.A. Saleh, in *Fundamentals of Photonics*, John, Wiley and Sons, 1991, ch. 17, pp. 644-695.
- <sup>67</sup> Please refer to reference -67
- <sup>68</sup> "Microchannel plate", <http://www.iuac.res.in/atmol/~safvan/mridulathesis/node21>, (accessed 24/04/17).
- <sup>69</sup> Please refer to reference -35
- <sup>70</sup> Photocathode Technology, <http://www.hamamatsu.com/jp/en/technology/innovation/photocathode/index.html>, (accessed on 24/04/17).
- <sup>71</sup> Photomultiplier Tubes, [http://psec.uchicago.edu/links/pmt\\_handbook\\_complete.pdf](http://psec.uchicago.edu/links/pmt_handbook_complete.pdf),

---

(accessed 24/04/17).

<sup>72</sup> Photomultiplier, <https://en.wikipedia.org/wiki/Photomultiplier>, (accessed 25/04/17).

<sup>73</sup> E.J. Sternglass *et al.*, *Rev. Sci. Instr.*, 1955, **26**, 1202.

<sup>74</sup> E.J. Sternglass *et al.*, *IRE Trans. Nucl. Sci.*, 1956, **3**, 29–32.

<sup>75</sup> M.M. Wachtel *et al.*, *Rev. Sci. Instrum.*, 1960, **31**, 576.

<sup>76</sup> E.J. Sternglass *et al.*, *IRE Trans. Nucl. Sci.*, 1962, **9**, 97–102.

<sup>77</sup> Lin *et al.*, *MRS Bulletin*, 2014, **39**, 533-541.

<sup>78</sup> J.E. Yater *et al.*, *Appl. Surf. Sci.*, 2002, **191**, 52–60.

<sup>79</sup> J.E. Yater *et al.*, *J. Appl. Phys.*, 2003, **93**, 3082–3090.

<sup>80</sup> Please refer to reference -9

<sup>81</sup> J.E. Yater *et al.*, *Diamond Relat. Mater.*, 2011, **20**, 798–802.

<sup>82</sup> H. Van der Graaf *et al.* *Inst. Methods Phys. Res. A*, 2016, accepted for publication.

<sup>83</sup> Please refer to reference -18

<sup>84</sup> R.T. Tung, *Applied Physics Reviews.*, 2014, **1**, 011304.

<sup>85</sup> J. Bardeen, *Physical Review.*, 1947, **71**, 717.

<sup>86</sup> A. Stadler, *Materials*, 2012, **5**, 661–683.

<sup>87</sup> J.E. Yater, *J. Appl. Phys.*, 2000, **87**, 8103–8112.

<sup>88</sup> J.B. Miller, G.R. Brandes, *J. Applied Physics*, 1997, **82**, 4538.

<sup>89</sup> C. Kittel, *Introduction to Solid State Physics*, Wiley, 7th Edition.

<sup>90</sup> B.S. Mitchell, in *An introduction to materials engineering and science: for chemical and materials engineers*, John Wiley & Sons, Inc., Hoboken, New Jersey, 2004, chapter 1, p. 59.

<sup>91</sup> Diamond structure,  
[http://www.open.edu/openlearn/ocw/mod/oucontent/view.php?printable=1&id=20276&extra=thumbnail\\_idp3183552](http://www.open.edu/openlearn/ocw/mod/oucontent/view.php?printable=1&id=20276&extra=thumbnail_idp3183552), (accessed 24/04/17).

<sup>92</sup> Crystal structure,  
<http://www.open.edu/openlearn/ocw/mod/oucontent/view.php?id=20276&printable=1>, (accessed 24/04/17).

<sup>93</sup> A.T. Collins, *Philosophical Transactions of the Royal Society A.*, 1993, **342**, 233–244.

- 
- <sup>94</sup> J.P. Goss, R.J. Eyre and P.R. Briddon, in *Physics and Applications of CVD Diamond*, Wiley-VCH, Weinheim, 2008, Theoretical models for doping diamond for semiconductor applications.
- <sup>95</sup> T.H. Borst, *Diamond and Related Materials*, 1995, **4**, 948-953.
- <sup>96</sup> G.E. Harlow, *The nature of diamonds*, Cambridge University Press., Cambridge, 1998, pp. 223;230–249.
- <sup>97</sup> David R. Lide (ed), in *CRC Handbook of Chemistry and Physics*, CRC Press., Boca Raton, Florida, 2003, 84th Edn, Section 12, Properties of Solids; Thermal and Physical Properties of Pure Metals.
- <sup>98</sup> K.E. Spear and J.P. Dismukes, *Synthetic Diamond: Emerging CVD Science and Technology*, John Wiley & Sons, Chichester, UK, 1994.
- <sup>99</sup> R. Locher *et al.*, *Appl. Phys. Lett.*, 1994, **65**, 34.
- <sup>100</sup> W. Zhu *et al.*, *J. Appl. Phys.*, 1995, **78**, 2707.
- <sup>101</sup> A. Tarun *et al.*, *Diamond & Related Materials*, 2016, **63**, 169–174.
- <sup>102</sup> A. Secroun *et al.*, *Phys. Status Solidi*, 2007, **204**, 4298–4304.
- <sup>103</sup> Please refer to reference -103
- <sup>104</sup> Please refer to reference -83
- <sup>105</sup> F.P. Bundy, *Journal of Geophysical Research*, 1979, **85**, 6930-6936.
- <sup>106</sup> *J. Mater. Chem.*, 2002, **12**, 2843–2855.
- <sup>107</sup> P. Cannon, *J. Am. Chem. Soc.*, 1962, **84**, 4253.
- <sup>108</sup> R. Abbaschian, *Diamond and Related Materials*, 2005, **14**, 1916–1919.
- <sup>109</sup> Please refer to reference -109
- <sup>110</sup> W.G. Eversole, Synthesis of Diamond, 1958, US Patent No. 3030187 and 3030188.
- <sup>111</sup> B.V. Derjaguin *et al.*, *Journal of Crystal Growth*, 1968, **2**, 380-384.
- <sup>112</sup> J.C. Angus, *Journal of Applied Physics*, 1968, **39**, 2915.
- <sup>113</sup> D.J. Poferl, *Journal of Applied Physics*, 1973, **44**, 1428.
- <sup>114</sup> M.N.R. Ashfold, P.W. May, C.A. Rego, *Chem. Soc. Rev.*, 1994, **23**, 21.
- <sup>115</sup> M. Schwander, K. Partes, *Diamond & Related Materials*, 2011, **20**, 1287–1301.
- <sup>116</sup> P.K. Bachmann, *Diam. Relat. Mater.*, 1991, **1**, 1.
- <sup>117</sup> Please refer to reference -119

- 
- <sup>118</sup> A. Argoitia, C.S. Kovach and J.C. Angus, in *Handbook of Industrial Diamonds and Diamond Films*, 1998, chapter 20, pp. 797-81.
- <sup>119</sup> J.E. Butler et al., *Philosophical Transactions of The Royal Society A*, 1993, **342**, 209-224.
- <sup>120</sup> S. Skokov *et al.*, *Physical Review B*, 1994, **49**, 5662-5671.
- <sup>121</sup> S. Koizumi *et al.*, *Applied Physics Letters*, 1997, **71**, 1065-1074.
- <sup>122</sup> R. Vaz, PhD Thesis, University of Bristol, 2013.
- <sup>123</sup> S.J. Harris, *Applied Physics Letters*, 1990, **56**, 2298-2301.
- <sup>124</sup> P.W. May, *Philosophical Transactions of Royal Society London A*, 2000, **358**, 474-494.
- <sup>125</sup> Please refer to reference -125
- <sup>126</sup> S. Matsumoto, *Japanese Journal of Applied Physics*, 1982, **21**, L183-L185.
- <sup>127</sup> F.G. Celii and J.E. Butler, *Annual Review of Physical Chemistry*, 1991, **42**, 643-684.
- <sup>128</sup> M.N.R. Ashfold *et al.*, *Physical Chemistry Chemistry Physics*, 2001, **3**, 3471-3485.
- <sup>129</sup> J. Zimmer and K.V. Ravi, *Diamond and Related Materials*, 2006, **15**, 229-233.
- <sup>130</sup> J. Cifre *et al.*, *Diamond and Related Materials*, 1992, **1**, 500-503.
- <sup>131</sup> Please refer to reference -109
- <sup>132</sup> M. Kamo, *J. Cryst. Growth*, 1983, **62**, 642.
- <sup>133</sup> Y. Saito, *J. Mater. Sci. Lett.*, 1986, **5**, 568.
- <sup>134</sup> V.V.S.S. Srikanth and X. Jiang, in *Synthetic diamond films: preparation, electrochemistry, characterization and applications*, ed. E. Brillas and C.A. Martínez-Huitle, John Wiley & Sons, Hoboken, NJ, USA, 2011, chapter 2, pp. 21-55.
- <sup>135</sup> B. Massarani, *Phys. Rev. B*, 1978, **17**, 1758.
- <sup>136</sup> K. Nishimura, *J. Appl. Phys.*, 1991, **69**, 3142.
- <sup>137</sup> A.T Collins, *Journal of Physics C: Solid State Physics*, 1971, **4**, 1789-1800.
- <sup>138</sup> T. Makino, *Diamond and Related Materials*, 2005, **14**, 1995 – 1998.
- <sup>139</sup> W.L. Wang, *Journal of Applied Physics*, 1996, **80**, 1846- 1851.
- <sup>140</sup> P. Wurzinger, *Diamond and Related Materials*, 1997, **6**, 763-768.

- 
- <sup>141</sup> D.W. Comerford *et al.*, *Journal of Physical Chemistry A*, 2006, **110**, 2868-2875.
- <sup>142</sup> A. Cheesman *et al.*, *Physical Chemistry Chemical Physics*, 2005, **7**, 1121-1126.
- <sup>143</sup> R. Samlenski, *Diamond and Related Materials*, 1996, **5**, 947-951.
- <sup>144</sup> Please refer to reference -5
- <sup>145</sup> D. Takeuchi, *Diam. Relat. Mater.*, 2008, **17**, 986.
- <sup>146</sup> S.Y. Chen, *New Journal of Physics*, 2002, **4**, 79.1-79.7.
- <sup>147</sup> Please refer to reference -125
- <sup>148</sup> S. Wang, *Diamond & Related Materials*, 2009, **18**, 669-677.
- <sup>149</sup> Please refer to reference -83
- <sup>150</sup> SEM, <https://www.jeol.co.jp/en/science/sem.html>, (accessed 26/04/17).
- <sup>151</sup> D.J. Gardiner, *Practical Raman spectroscopy*, Springer-Verlag, 1989.
- <sup>152</sup> J. Loader, *Basic Laser Raman Spectroscopy*, Heyden & Son Ltd., 1970.
- <sup>153</sup> R.J. Nemanich, *Journal of Vacuum Science and Technology A*, 1988, **6**, 1783-1787.
- <sup>154</sup> D.S. Knight, W.B. White, *Journal of Materials Research*, 1989, **4**, 385.
- <sup>155</sup> J. Filik, *Spectroscopy Europe*, 2005, **17**.
- <sup>156</sup> P. Ascarelli, *Applied Surface Science*, 1993, **64**, 307-311.
- <sup>157</sup> P.W. May *et al.*, *Diamond & Related Materials*, 2008, **17**, 105-117.
- <sup>158</sup> Raman Spectra Assignment,  
<http://www.horiba.com/fileadmin/uploads/Scientific/Documents/Raman/bands.pdf>,  
(accessed 25/04/17).
- <sup>159</sup> J.S. Burgess *et al.*, *Carbon*, 2008, **46**, 1711-1717.
- <sup>160</sup> A. Denisenko *et al.*, *IEEE Transactions Nucl. Sci.*, 1996, **43**, 3081-3088.
- <sup>161</sup> A. Denisenko *et al.*, *Diamond Films and Technol.*, 1995, **5**, 189-197.

---

Thank you very much for reading this work.  
I hope it was enjoyable and enlightening!

Christine